IEEE Transactions on Quantum Engineering

Received 1 August 2022; revised 15 February 2023; accepted 2 March 2023; date of publication 10 March 2023; date of current version 11 April 2023.

Digital Object Identifier 10.1109/TQE.2023.3255743

On Noise-Sensitive Automatic Tuning of Gate-Defined Sensor Dots

FABIAN HADER[1], JAN VOGELBRUCH[1], SIMON HUMPOHL[2], TOBIAS HANGLEITER[2], CHIMEZIE EGUZO[1], STEFAN HEINEN[1], STEFANIE MEYER[1], AND STEFAN VAN WAASEN[1,3]

[1]Central Institute of Engineering, Electronics and Analytics ZEA-2 – Electronic Systems, Forschungszentrum Jülich GmbH, 52425 Jülich, Germany

[2]JARA-FIT Institute for Quantum Information, Forschungszentrum Jülich GmbH and RWTH Aachen University, 52074 Aachen, Germany

[3]Faculty of Engineering – Communication Systems, University of Duisburg-Essen, 47057 Duisburg, Germany

Corresponding author: Fabian Hader (e-mail: f.hader@fz-juelich.de).

This work was supported by the Impulse and Networking Fund of the Helmholtz Association.

ABSTRACT In gate-defined quantum dot systems, the conductance change of electrostatically coupled sensor dots allows the observation of the quantum dots' charge and spin states. Therefore, the sensor dot must be optimally sensitive to changes in its electrostatic environment. A series of conductance measurements varying the two sensor-dot-forming barrier gate voltages serve to tune the dot into a corresponding operating regime. In this article, we analyze the noise characteristics of the measured data and define a criterion to identify continuous regions with a sufficient signal-gradient-to-noise ratio. Hence, accurate noise estimation is required when identifying the optimal operating regime. Therefore, we evaluate several existing noise estimators, modify them for 1-D data, optimize their parameters, and analyze their quality based on simulated data. The estimator of Chen et al. turns out to be best suited for our application concerning minimally scattering results. Furthermore, using this estimator in an algorithm for flank-of-interest classification in measured data shows the relevance and applicability of our approach.

INDEX TERMS Automated tuning, charge sensor, noise estimation, quantum computing, semiconductor quantum dots.

I. INTRODUCTION

Quantum dots are a promising scalable platform for quantum computations. However, the isolation of electrons in quantum dots is a nontrivial task that needs to be automated. One can observe the charge and spin states in gate-defined quantum dots by the conductance change of a nearby electrostatically coupled sensor dot. It is optimally sensitive if the sensor dot gate voltages reach a particular operating regime during the tuning. To locate the operating point, we carry out reflectometry measurements[1] of the conductance through the sensor dot while varying the barrier gate voltages, SL and SR, forming the sensor dot. This measured signal, proportional to the conductance $G_m(SL, SR)$, comprises the undisturbed sensor dot signal overlayed with some noise. Thus, as part of the autotuning development, our primary focus is to identify continuous regions with sufficient signal-gradient-to-noise ratio.

Fig. 1 illustrates the methodological procedure of our investigation. Section II-A covers the tuning procedure and the requirements for suitable voltage regions. The noise characteristics must be accurately estimated when identifying the optimal operating regime. Many noise estimators exist for 2-D data applications (see Section II-B). However, as our sensor dot data sampling is highly anisotropic, the estimation can only be performed on 1-D data. Thus, only estimators that are adaptable to 1-D come into consideration. Furthermore, a quantitative analysis of the estimator results requires a known ground truth. Therefore, an inevitable first step is to analyze the noise sources and generate a theoretical model. Then, generated realistic sample data, composed of simulated noise and approximated clean sensor dot data, constitute the ground truth. Sections III-A–III-D cover the noise analysis and generation of data.

[1]Although in our work reflectometry measurements are performed, the results should also be transferable to other measurement techniques (e.g. DC).

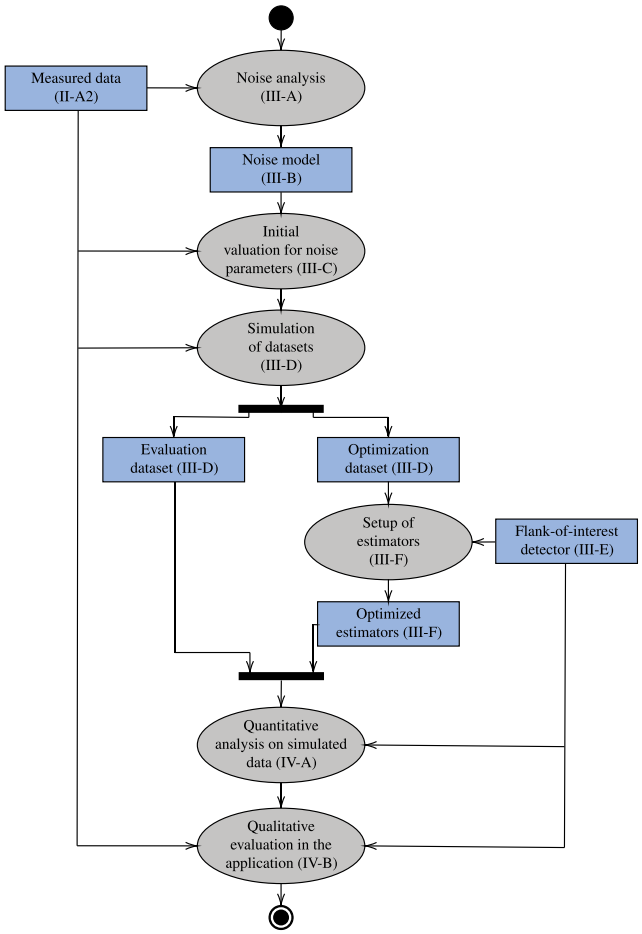

FIGURE 1. Activity diagram of the methodological procedure. The numbers in brackets refer to the associated section.

After quantitatively comparing the estimators with simulated data in Section IV-A, the qualitative evaluation in Section IV-B analyzes the impact of the estimators' characteristics on the detection of qualified regions in measured data.

II. BACKGROUND

A. SENSOR DOT TUNING

Semiconductor gate-defined quantum dot systems often incorporate charge sensors to measure the quantum dot's charge state, which allows accessing dot parameters such as capacitive coupling and tunnel coupling. Moreover, the electron spin which is typically used to encode and process quantum information can be read out via spin-to-charge conversion [1].

One way to realize a charge sensor is a capacitively coupled quantum dot called a sensor dot. In the correct operating regime, changes in the local electrostatic environment directly affect the conductance through the sensor dot [2], thus providing measurement information about the quantum dot's charge state. The key to tuning a sensor dot is to observe the energy of the dot via its conductance characteristics as a function of the applied gate voltages [3].

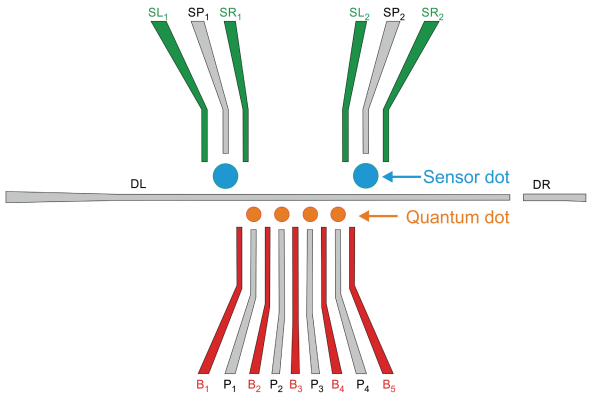

FIGURE 2. Arrangement of the sensor dot gates. Blue spots mark sensor dot regions and orange spots quantum dot areas. The gates SL_1, SP_1, and SR_1 form the left sensor dot, and the gates SL_2, SP_2, and SR_2 the right one.

TABLE 1. Most Relevant Noise Sources in Quantum Dot Systems

Noise type	Noise source	Characteristics
Charge noise	Fluctuating charges in the heterostructure	Pink, Gaussian
Johnson-Nyquist noise	Thermal agitation of the charge carriers in the amplifier	White, Gaussian

For the present experiment, Fig. 2 illustrates the arrangement of the gates that form the regions for the sensor and the quantum dots. The authors in [4] and [5] describe the overall experiment setup, and Fig. 3 shows the schematic representation of the signal path.

The works mentioned report on two types of existent noise that are relevant for this work: 1) charge noise and 2) thermal noise (see Table 1). According to the work in [6], charge noise shows pink characteristics. For pink noise, also known as $1/f$-noise, the power spectral density is proportional to $f^{-\alpha}$ with typically $0.5 \lesssim \alpha \lesssim 2$ [7], [8], [9]. On the other hand, thermal noise, also known as Johnson–Nyquist noise, is approximately white and has a nearly Gaussian amplitude distribution if limited to a finite bandwidth [10]. Therein, white denotes a constant noise power spectral density.

1) SENSOR DOT PREPARATION

This work focuses on criteria to ultimately evaluate the eligibility of Coulomb peaks. Therefore, this analysis requires that the sensor dot has been formed, i.e., Coulomb oscillations[2] are visible in barrier–barrier scans. This requires numerous device-dependent tuning steps, which for our device are as follows.

1) Deplete 2DEG below *DL*/*DR* to split the sample in sensing and computation region.

[2]Coulomb oscillations are voltage-dependent oscillations in conductance through a quantum dot.

IEEE Transactions on Quantum Engineering

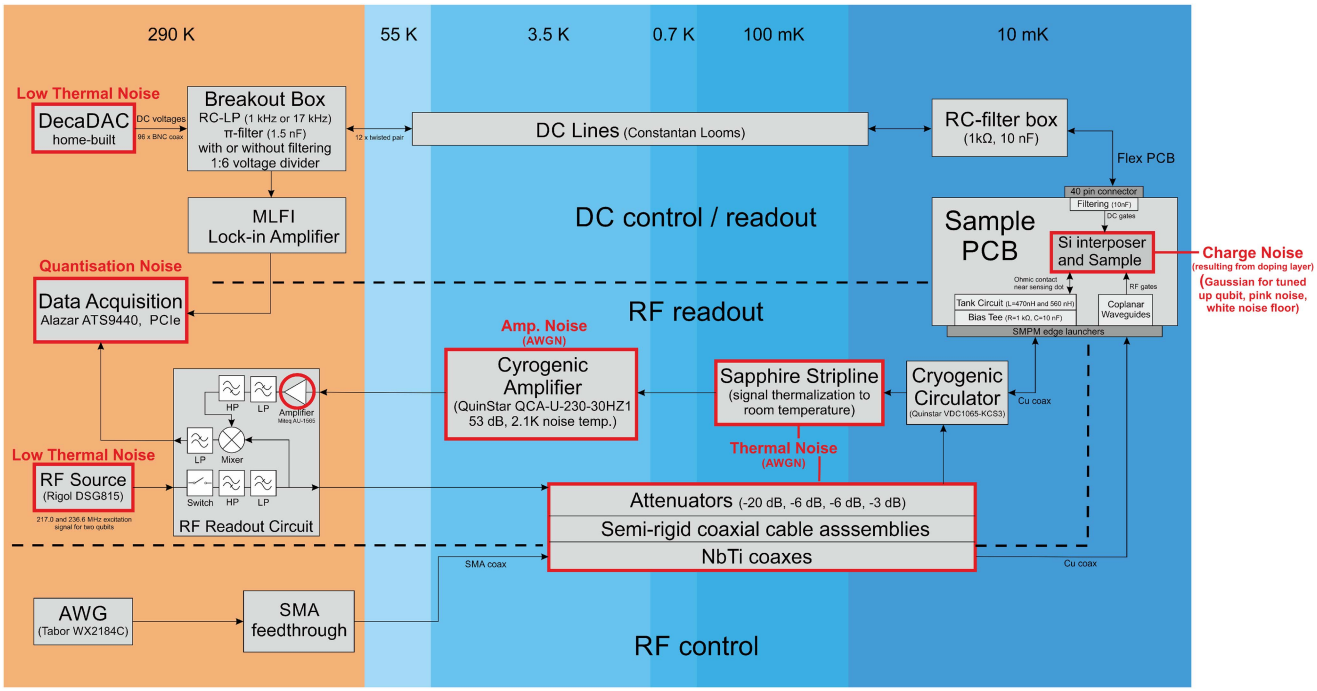

FIGURE 3. **Diagram of the signal path. The sample printed circuit board (PCB) contains the current sample with the gates for the sensor dots and quantum dots. In the dc part, a digital-to-analog converter (DecaDAC) processes and generates the gate voltages. Then, the breakout box filters these voltages before arriving at the area cooled to 55 K. Here, 12 twisted pairs of dc lines (Constantan looms) transmit the signals to the *RC* filter box, which operates at only 10 mK. After filtering, the voltages reach the gates on the sample PCB. The radio frequency (RF) part implements a homodyne detection setup. A single tone generated by an RF source is sent via a coaxial cable and a circulator to the sample PCB where it is matched to the sensor dot impedance by an *LC* tank circuit. The circulator directs the signal reflected at the sample to a second coaxial cable. This signal is thermalized by a sapphire stripline and amplified at 3.5 K and at room temperature, where it is demodulated, low-pass filtered, and finally digitized using a PCI Express card.**

2) Pick a voltage for the plunger SP_i of sensor dot $i = 1, 2$ (see Fig. 2) from a priori knowledge.
3) Test if Coulomb oscillations are visible in barrier–barrier (SL_i/SR_i) scans. If not, go back to 2. Otherwise, select the voltage range with Coulomb oscillations.

The last step relies on wide-scan measurements using the same measurement principle as described in Section II-A2 for the narrow scans. The exemplary scan in Fig. 4 covers a wide voltage range to determine the area with Coulomb oscillations (red box). Promising approaches for its localization include the application of the following:

1) classical image processing methods comprising the following:
   a) the Gabor filter [11];
   b) region growing, edge detection, K-means clustering with contouring, and template matching [12];
2) object detection with deep learning [12], [13], [14].

After performing the above steps, the measurement of the narrow scan data described in Section II-A2 enables the analysis presented in this work.

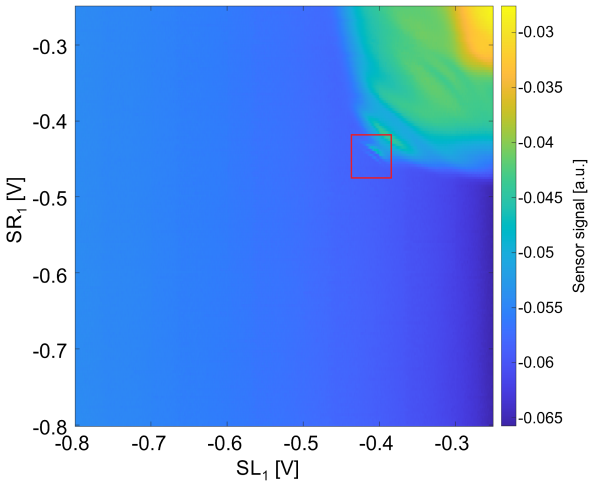

FIGURE 4. **Wide-scan data of a sensor dot with a red box marking the area of interest that contains the Coulomb oscillations. In this area, a sensor dot has been formed and can be further adjusted.**

2) SENSOR DOT NARROW SCANS

Predominantly, the conductance characteristics of sensor dots $G_{sd}(SL, SR)$ represented in a sensor dot scan are controlled via the two barrier gate voltages (SL_i and SR_i for sensor dot $i = 1, 2$ in Fig. 2). A fine or narrow scan in the

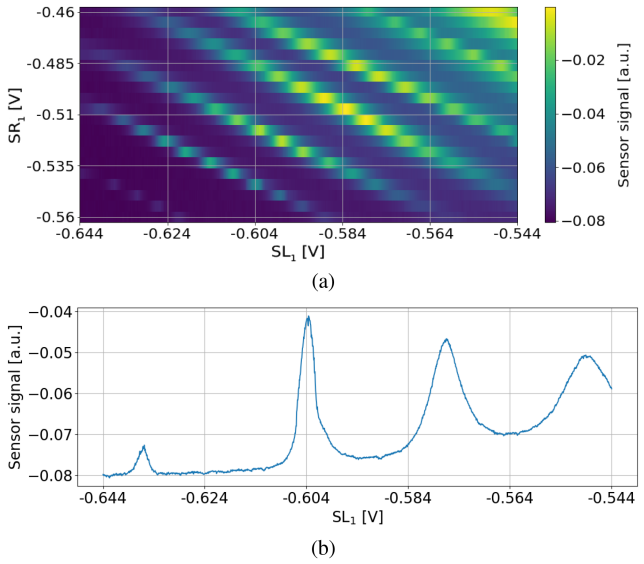

FIGURE 5. Example data from sensor dot measurements. (a) Sensor dot narrow scan data. (b) Row data of the narrow scan in (a) with $SR_1 = -0.544$ V.

region with Coulomb oscillations [shown in Fig. 5(a)] sufficiently resolves the oscillations to determine an optimal sensor dot working point. These narrow scans are of interest to the present work.

Due to the experimental setup and measurement time reduction, the voltage on one axis changes stepwise. The other voltage continuously ramps up in a defined voltage interval while an integration generates the measurement data. In our experiments, a narrow scan typically delivers 10 or 20 rows of data consisting of 1664 data points each. This distinct anisotropic 2-D data resolution requires a rowwise data analysis to avoid artifacts. Fig. 5(b) shows a 1-D data example of a single row.

3) REQUIREMENTS

To provide an optimal operating point, the requirements for a qualified region are as follows:

1) a steep slope to achieve the strongest possible response and sensitivity[3] [4], [15];
2) adequate linearity of the slope to achieve a constant behavior within the region;[4]
3) a large region or rather a wide voltage range to have as much flexibility as possible when the working point shifts;
4) a sufficient signal-gradient-to-noise ratio.

The operation point selection is sensitive to the last requirement and, thus, requires precise noise estimation. Therefore, we propose the minimal signal gradient (MSG) criterion to ensure a sufficient signal-gradient-to-noise ratio in a qualified region

$$\mathrm{MSG} = \epsilon \cdot \sigma \cdot \frac{\Delta V}{V_{\min}} \tag{1}$$

where σ denotes the standard deviation (STD) of the estimated noise, ΔV the voltage sample distance, $V_{\min}$ the minimal required voltage resolution of the sensor dot, and ϵ the desired signal-gradient-to-noise factor. Fig. 6 shows a visualization of the MSGs composition. For a Gaussian distribution, 99.73% of the noise is in the range of 3σ. We choose a value of 10 for ϵ, resulting in an additional security distance of 4σ between two measurement points. The term $\frac{\Delta V}{V_{\min}}$ relates the minimal required voltage resolution to sample points. Thus, if the gradient in a qualified region is always greater than the MSG, the signal change for each $V_{\min}$ is at least ϵ times as large as the noise σ.

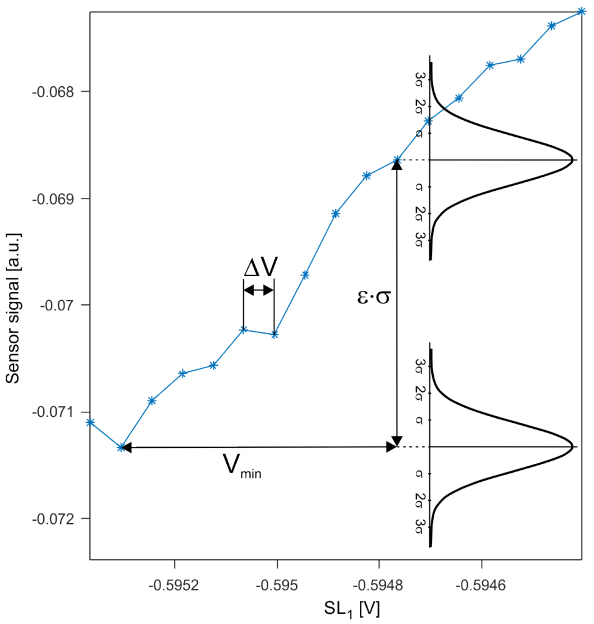

FIGURE 6. Visualization of the MSG criterion (1) with ϵ: desired signal-gradient-to-noise factor, σ: estimated noise STD, ΔV: voltage sample distance, and $V_{\min}$: minimal required voltage resolution of the sensor dot.

B. NOISE ESTIMATION

Noise estimation is still a highly discussed topic in data analysis and processing. In signal processing, noise refers to unknown, unwanted distortions a signal may experience during acquisition, storage, transmission, processing, or conversion [16]. From the estimation theory viewpoint [17], [18], our 1-D measurement (the observation) is regarded as one realization of a sensor measurement (the random process). The parametric model described in Section III-B (the observation model) translates our a priori knowledge on the data. Primarily, our statistical signal part consists of Gaussian distributions (the probability laws) described by parameters. The task of the estimation is to find an approximate value

[3] A steep slope as a function of the gate voltage corresponds to a steep slope as a function of the change of the electrostatic potential, which is the parameter to be measured later on.

[4] Automatic analysis can benefit from a linear response, e.g., for background compensation.

for the parameters. In our case, only the estimation of the final noise amplitude's STD in the 1-D data is required for the MSG criterion in (1).

However, existing state-of-the-art estimators often specialize in a particular application and data dimensionality. Therefore, to evaluate the estimators, we collect them, examine their adaptability to 1-D space, and, if possible, revise them. The following sections provide a classification overview on different noise estimation approaches. A more general insight into different noise estimators can be found in [19], [20], [21], [22], and [23].

1) SPATIAL DOMAIN APPROACHES

Approaches that work with spatial domain analysis apply the following:

1) local filtering techniques [24] and statistical analysis using the following:
   a) the Laplacian filter [25];
   b) Laplacian and gradient data masks [26];
   c) a modified Gaussian filter [27];
   d) the ROAD-statistic-based impulse detector [28];
2) truncated local Taylor series approximation [29];
3) a step signal model utilizing polarized derivatives and their nonlinear combination [30];
4) a minimally controlled recursive averaging technique and neighborhood analysis [31];
5) Mahalanobis distance measure from multivariate empirical mode decomposition [32];
6) a difference prefiltering and statistical evaluation of a histogram of local signal variances [33];
7) singular value decomposition (tail part) and content-dependent parameter determination [21].

2) PATCH-BASED APPROACHES

Patch-based approaches subdivide the data into homogeneous regions (patches, blocks, or superpixels). Patches are analyzed with different approaches using the following:

1) the mean of local variance of homogeneous regions [34];
2) a gradient approach (Laplace) [35];
3) the Sobel filter and an averaging filter [36];
4) Kendall's τ [37], [38];
5) principal component analysis [39] applying for patch selection:
   a) static [40], [41] and adaptive [42] thresholding or statistics of the patches' local variance [43];
   b) a multidirectional high-pass operator as uniformity estimator followed by the calculation of a quantity threshold of homogeneity measure [44];
   c) the eigenvalues of the gradient covariance matrix of the patches [45], [46];
   d) the statistical relationship between the noise variance and the eigenvalues of the covariance matrix of patches [47];
   e) an iterative strategy to adaptively choose the optimal set of patches [48], [49], [50].

3) TRANSFORM-BASED APPROACHES

The methods in this category apply the transformation of the given data with different approaches for noise identification:

1) wavelet decomposition [51], [52], [53];
2) trained moments and cumulative distribution functions of wavelet components [54];
3) goodness-of-fit test on dual-tree complex wavelet transform coefficients [55];
4) Morrison noise reduction method [56];
5) discrete cosine transformation [57], [58], [59], [60]:
   a) with analysis of variance and kurtosis or [61];
   b) utilizing a thin-plate spline approximation [62].

III. EVALUATION PROCEDURE

A. NOISE ANALYSIS

To evaluate the estimators, we need to analyze the nature of the existing noise to construct simulated data as the ground truth. Random fluctuations and telegraph noise [63] are not of interest here. Moreover, dedicated algorithms have to detect them and reject contaminated flanks.

For noise analysis, a common strategy is to separate the noise from the signal by reconstructing the initial signal. However, various problems arise when fitting the signal with Lorentzians [64], the well-known behavior of Coulomb oscillations [65]. Usually, the fit works well for single peaks not influenced by neighboring peaks. However, peaks overlap in most of our data, challenging a suitable fit. Notably, the peak position is unknown for incomplete oscillations at the signal borders. We also observe several other distortions diverging from the Lorentzian model, including an overall signal drift, oscillations in the signal [see Fig. 7(a)], and peaks that do not conform to the expected shape [see Fig. 7(b)]. Moreover, fitting with Lorentzians is considerably more time-consuming, as the dimensionality of the optimization problem increases with the number of peaks and sometimes requires manual adjustments.

Therefore, we follow a general, fully automatic approach to extract the noise. First, we perform 1-D Gaussian smoothing followed by a spline interpolation to ensure signal steadiness. Then, we subtract the approximated signal from the original signal to reveal a first assessment of the present noise, as visible in Fig. 8. The example suggests that the noise characteristic is not homogeneous but depends on the signal regime.

To further investigate the signal dependence of the noise, we perform a local noise estimation using the methods of Chen et al. [47] [5] and Donoho [52] in a sliding window. Its size should balance sufficient statistics for a robust estimate with enough local significance. Therefore, we choose a window size of 201, considering the confidence intervals for

[5]With a patch size of 6.

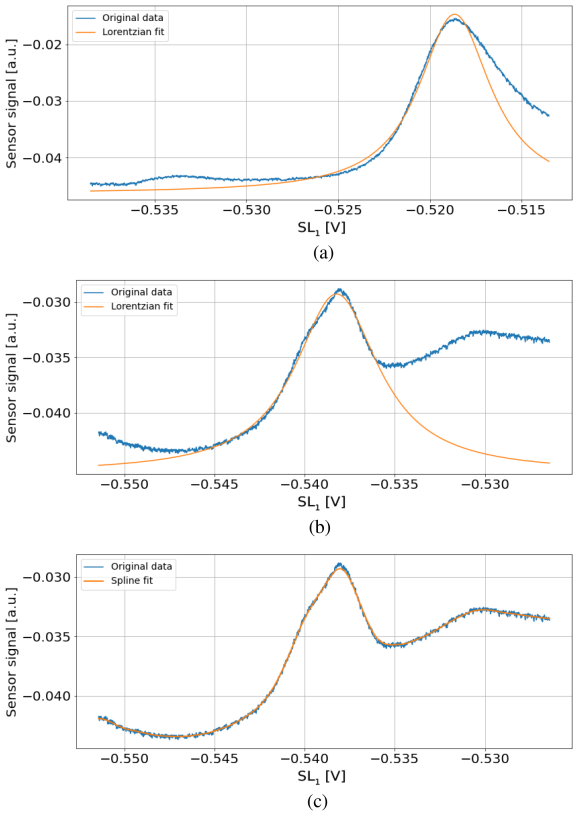

FIGURE 7. Examples of problems when applying a fit with Lorentzians. (a) Oscillations in the signal and missing information about the influence of the next peak. (b) Unexpected peak shape and substantial interference between peaks. (c) Same data fit as in (b) but using Gaussian smoothing and spline interpolation.

the STD of a draw from a normal distribution[6] (see Fig. 9). Within the local noise analysis framework, we could confirm more substantial local noise in the flanks and a more distinctive overall noise scattering compared to the pure additive white Gaussian noise (AWGN) case. Among others, these originate from distortions directly affecting the gate voltages or occurring in the sample and are amplified parametrically by the sensor.

B. NOISE MODEL

1) STANDARD MODEL

The simplified generic model of the measured signal G_m consists of an idealistic noise-free signal G_{sd} at the sensor dot and additive noise n, including all noise sources

$$G_m(SL, SR) = G_{\text{sd}}(SL, SR) + n\,. \tag{2}$$

n is composed of the gradient-dependent noise (n_{grad}) before and the constant noise (n_{const}) after the dot

$$\begin{aligned} n &= n_{\text{grad}} + n_{\text{const}} \\ &= X_{\text{grad}} \cdot \frac{\partial}{\partial SL} G_{\text{sd}}(SL, SR) + X_{\text{const}} \end{aligned} \tag{3}$$

[6]Calculated using the chi-squared distribution.

with X_{grad} and X_{const} representing random variables for the noise distributions. According to Section II-A, we presume pink noise for n_{grad} and white noise for n_{const}. The amplitude of the individual noise sources is sufficiently independent and normally distributed. Based on the central limit theorem, we summarize both types of noise as one normal distribution. This results in the following representation:

$$\begin{aligned} X_{\text{grad}} &\sim \mathcal{N}(0,\ \sigma^2_{\text{grad}}) \\ X_{\text{const}} &\sim \mathcal{N}(0,\ \sigma^2_{\text{const}}) \end{aligned} \tag{4}$$

with σ being the STD of the corresponding noise in the system. Because X_{grad} influences the applied voltages, it is multiplied by the signal gradient to obtain the measured noise n_{grad}. In a sufficient linear region, the corresponding STD $\hat{\sigma}_{\text{grad}}$ can be calculated

$$\hat{\sigma}_{\text{grad}} = \sigma_{\text{grad}} \cdot \frac{\partial}{\partial SL} G_{\text{sd}}(SL, SR)\,. \tag{5}$$

The STD of the total noise in the measurement data σ_n is composed of σ_{const} and $\hat{\sigma}_{\text{grad}}$

$$\sigma_n = \sqrt{\hat{\sigma}^2_{\text{grad}} + \sigma^2_{\text{const}}}\,. \tag{6}$$

2) EXTENDED MODEL

Although we found no clear evidence for the presence of linearly signal-dependent noise (n_{lin}) in the measured data, we extended our model by n_{lin}, as it occurs in many applications

$$\begin{aligned} G_m(SL, SR) &= G_{\text{sd}}(SL, SR) + n_{\text{grad}}(SL, SR) \\ &\quad + n_{\text{const}} + n_{\text{lin}}(SL, SR) \\ n_{\text{lin}}(SL, SR) &= X_{\text{lin}} \cdot G_{\text{sd}}(SL, SR) \\ X_{\text{lin}} &\sim \mathcal{N}(0,\ \sigma^2_{\text{lin}}) \\ \hat{\sigma}_{\text{lin}} &= \sigma_{\text{lin}} \cdot G_{\text{sd}}(SL, SR)\,. \end{aligned} \tag{7}$$

We assume n_{lin} to be approximately white. The extended model allows for evaluating the estimators for a broader possible application spectrum.

C. INITIAL VALUATION FOR NOISE PARAMETERS

We perform the first assessment for the different noise parts with the noise estimators of Donoho [52] and Chen et al. [47]. Flat areas with a low slope in the 1-D measurement signal $G_{m,\text{1-D}}(SL)$ qualify to determine an initial guess for σ_{const}, whereas in steep areas, we estimate σ_{est}. Then, we calculate an initial guess for σ_{grad}

$$\sigma_{\text{grad}} = \frac{\sqrt{\sigma^2_{\text{est}} - \sigma^2_{\text{const}}}}{\overline{\nabla G_{m,1D}}} \tag{8}$$

where $\overline{\nabla G_{m,1D}}$ denotes the average gradient of an area. Fig. 10 illustrates the results for the estimator of Donoho. Furthermore, Table 2 lists the corresponding centralized 95%-quantile ($\text{CQ}_{0.95}$) interval for σ_{const}, σ_{grad}, and $\hat{\sigma}_{\text{grad}}$. For the last, we multiply σ_{grad} with the average gradient of

IEEE Transactions on Quantum Engineering

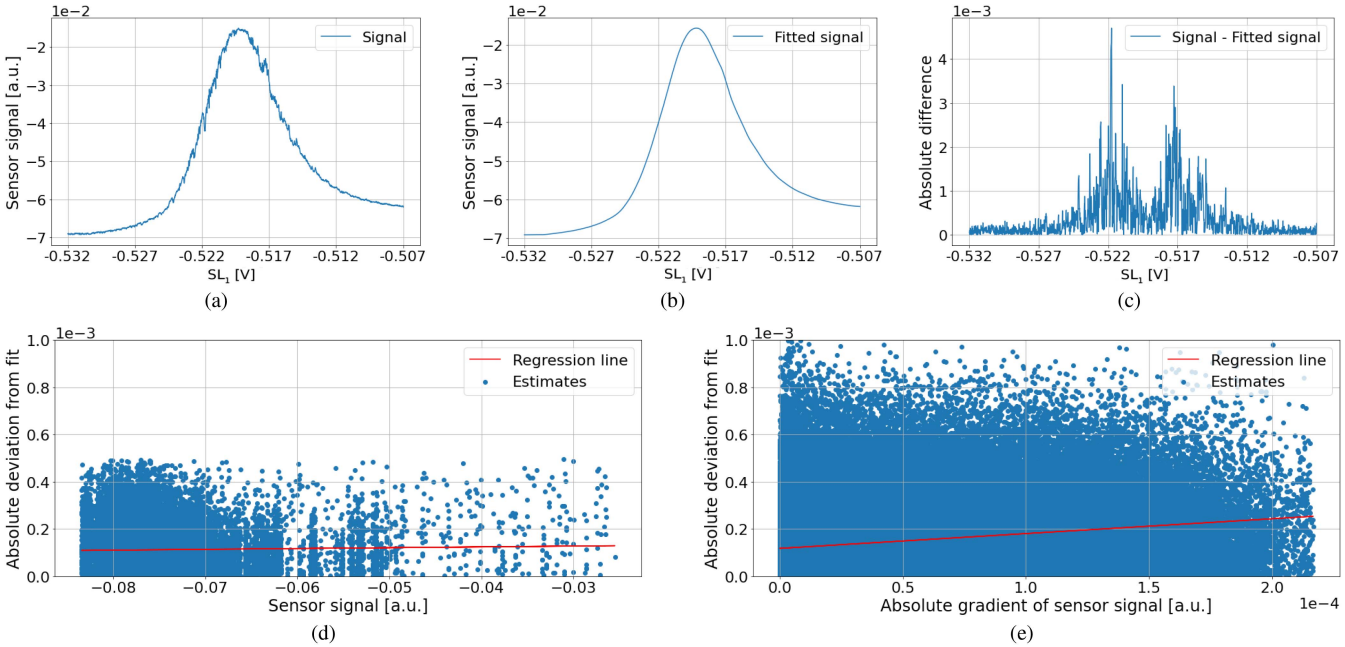

FIGURE 8. Initial noise analysis by fitting the signal and calculating the difference in fit with the original signal. Example showing (a) the signal, (b) the fitted version of the signal, and (c) the absolute difference between the signal and the fit. (d) Dependence of the noise on the sensor signal only in flat regions. Thus, we suppress the gradient-dependent parts. Signal peaks often cannot fulfill the flatness criterion, resulting in fewer estimates. The regression line shows a noise increase of 18.33% and does not indicate any relevant dependence. (e) Dependence of the noise on the sensor signal gradient. The regression line shows a clear dependence on the gradient, with an increase of 115.52%.

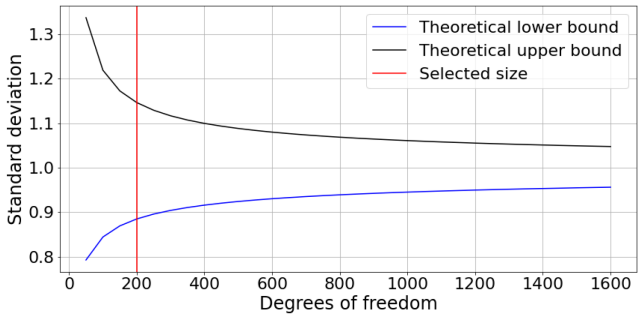

FIGURE 9. Theoretical confidence interval for the STD of 1 with alpha=0.01 and different degrees of freedom.

TABLE 2. Results of the Initial Valuation for Different Noise Types Using the Estimator of Donoho

Parameter	Value
$CQ_{0.95}$ interval for σ_{const}	$[8.6; 13.9] \cdot 10^{-5}$
$CQ_{0.95}$ interval for σ_{grad}	$[0.4; 4.7]$
$CQ_{0.95}$ interval for $\hat{\sigma}_{grad}$	$[1.4; 16.9] \cdot 10^{-5}$

the dataset (3.6×10^{-5}). Notably, the $\hat{\sigma}_{\text{grad}}$ interval scatters more than the σ_{const} interval, as the scattering of σ_{const} still affects the calculation of σ_{grad}. The estimator of Chen et al. produces similar results but with less scattering.

We also conduct an initial valuation for the n_{lin}. For this purpose, we consider different levels of flat regions to suppress n_{grad} and divide the estimates by the average signal of the corresponding region. Again, we cannot observe an existing n_{lin} of sufficient significance in these investigations.

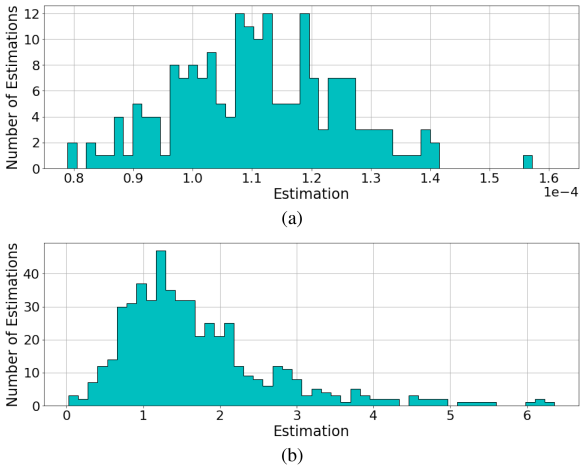

FIGURE 10. Histogram of the estimated initial guess for the noise distributions σ obtained using the estimator of Donoho. (a) Estimates for σ_{const}. (b) Estimates for σ_{grad}.

D. SIMULATION OF DATASETS

For our examination, we create two separate datasets. The first is to optimize the estimator parameters, and the second is to perform the quantitative analysis. The optimization dataset consists of 65 images and the evaluation dataset of 203 images. Both sets realize the standard and the extended noise model added to a fitted version of the measured signal. Table 3 gives an overview of the value ranges of the data and gates.

Starting with the initial guess (see Section III-C), we further optimize the noise generation parameters for each image

TABLE 3. Parameters of the Measured Data

Dataset	SL voltages [mV]	SL range [mV]	SL stepsize [mV]	SR voltages [mV]	SR range [mV]	Sensor signal [10^{-3} a.u.]
optimization	[-668.58, -398.03]	[25.00, 100.00]	[0.015, 0.060]	[-603.42, -442.69]	[25.00, 100.00]	[-84.85, 4.30]
evaluation	[-694.74, -508.68]	[25.00, 100.00]	[0.015, 0.060]	[-691.31, -404.08]	[25.00, 100.00]	[-75.56, 12.01]

The gate voltages used differ between individual scans, and the individual dynamic voltage range falls into the interval of the respective gate. The stepsize indicates the difference in voltage between two measuring points.

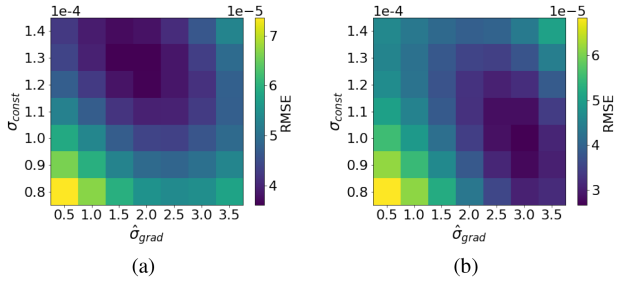

FIGURE 11. Optimization results of noise parameters for the standard noise model. Heat map of the RMSE of noise parameter combinations across all images for (a) the optimization dataset and (b) the evaluation dataset.

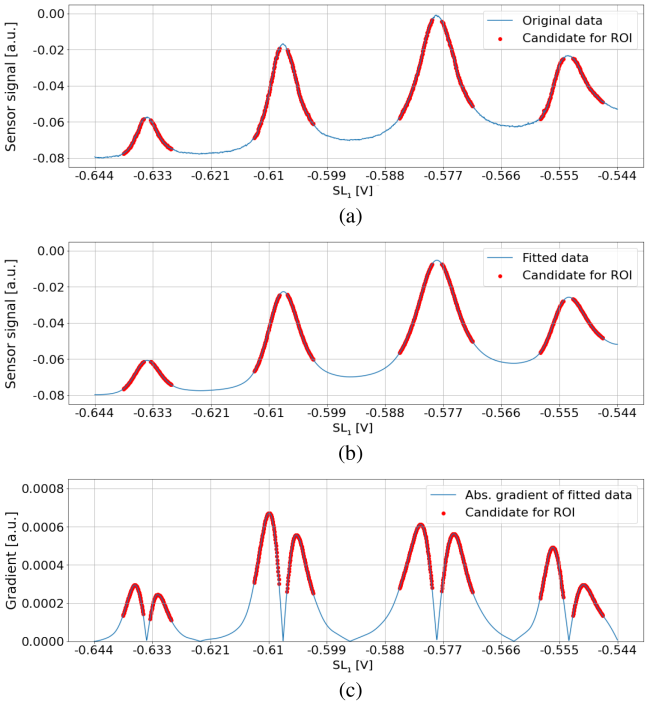

FIGURE 12. FOI detection: FOIs, defined by the minimal gradient, the minimal relative deviation from the local gradient maximum, and the minimal region size, are colored red. (a) Single row of measured data. (b) Fitted row. (c) Absolute gradient of the fitted row.

independently because of the scattering of their noise levels. The root-mean-square error (RMSE) between the locally estimated STD of the measured and the simulated data steers optimizing the regionally differing noise in the complete signal. We choose the estimator of Chen et al. to target a low variation of the estimates.[7] A PCG family[8] generator, known for its excellent performance in statistical tests [66], creates the AWGN part, whereas the algorithm from [67][9] produces the pink noise part.

Fig. 11 shows the optimization results for standard noise model parameter combinations. We generate the simulated datasets with the best combination per image.

E. FLANK OF INTEREST DETECTION

First, our flank-of-interest (FOI) detection algorithm calculates the absolute gradient of a fit to the measured data. Then, it selects maxima with a value of at least *discard_weak* times the value of the strongest one in the current row. Doing so dynamically prevents the inclusion of small maxima resulting from disturbances in the original signal. Next, around each selected maximum, the algorithm determines a candidate region defined by values higher than *increase_until* times the maximum. Finally, it records only candidate regions as FOIs with at least *min_size* data points determined from the sampling rate and a voltage range of 3 mV. Default values used for our sensor dot scans are as follows.

1) $min\_size = \lceil \frac{3\,\mathrm{mV}}{\Delta x} \rceil$.
2) $increase\_until = 0.5$.
3) $discard\_weak = 0.2$.

The example in Fig. 12 visualizes detected and selected edges in the signal.

F. SETUP OF ESTIMATORS

Table 4 gives an overview of the estimators considered in our work, their references, and the source code used. We only consider estimators adaptable to 1-D signals.

We use the simulated optimization dataset to optimize the parameters of the estimators. The cost function consists of the RMSE between the estimated and the actual STD of all detected FOIs. Instead of using the STD parameters of the noise generation, we calculate the actual STD of the added

[7]The data are not optimized for the estimator to estimate as accurately as possible, but to be as similar as possible to the real data. Thus, the estimator used has no advantage in the evaluation process by being used for data optimization. The underlying artificial noise and the accuracy of the estimation is not known to the estimator at any time.

[8]PCG64 from *NumPy*-module `random`.

[9]Implemented in the python library `colorednoise`

IEEE Transactions on Quantum Engineering

TABLE 4. Implementations of the Noise Estimators, Sorted by the Year of Publication

Estimator name	Year	Ref.	Source Code	Programming language
Olsen	1993	[24]	[68]	Matlab
DonohoJohnstone	1994	[51]	[69]	Matlab
Donoho	1995	[52]	[69]	Matlab
Immerkær	1996	[25]	[69]	Matlab
AbdelnourSelesnick	2000	[53]	[69]	Matlab
Garnett	2005	[28]	[70]	Matlab
Smith	2006	[56]	[56]	Matlab
D'Errico	2007	[29]	[29]	Matlab
TaiYang	2008	[35]	[68]	Matlab
ZoranWeiss	2009	[61]	[71]	Matlab
Garcia	2010	[62]	[72]	Matlab
YangTai	2010	[36]	[73]	Matlab
Liu	2012	[45]	[74]	Matlab
Laligant	2013	[30]	[68]	Matlab
Pyatykh	2013	[41]	[75]	Matlab
Chen	2015	[47]	[76]	Python
Sutour	2015	[38]	[77]	Matlab
Ponomarenko	2017	[59]	[78]	Matlab

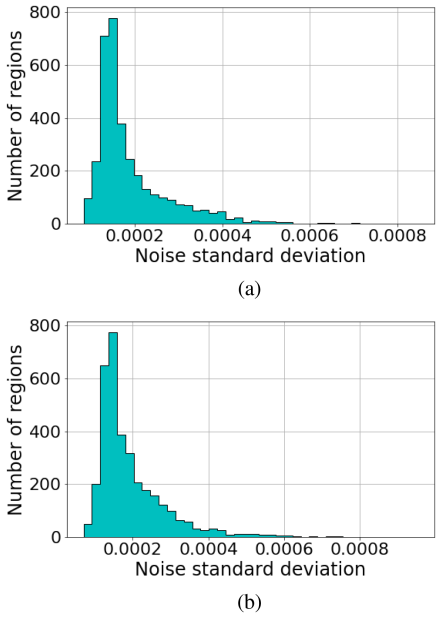

FIGURE 13. Histogram of the actual noise STD in an FOI for the evaluation dataset. (a) Standard noise model. (b) Extended noise model.

noise to improve the accuracy of the ground truth. Table 5 shows the best parameters used for the evaluation. Since we found the same best parameters for both noise models, we omit a further comparison between the models at this point.

TABLE 5. Results of the Noise Estimator Parameter Optimization

Estimator name	Parameters	Value
Olsen	Percentage of points having a low gradient to take into account	55.0
	.....	.....
	Averaging type (0='lms'; 1='mean')	1.0
Smith	Maximum number of iterations to use in the Morrison denoising method	1.0
TaiYang	Threshold for excluding structures and details after edge detection	100.0
ZoranWeiss	Patch size	4.0
YangTai	Threshold for excluding structures and details after edge detection	1.0
Liu	Patch size	2.0
Pyatykh	Patch size	6.0
Chen	Patch size	3.0
Ponomarenko	Number of DCT coefficients of each image block to be used for further analysis	4.0

Although initially working in manually selected regions, the *YangTai* and *Sutour* approaches are not applicable because their internal homogeneity criteria do not match the characteristics of our data. Therefore, we exclude these estimators from further evaluation. Due to similar reasons, the *Liu* estimator only enters its first iteration in the estimation process. However, we maintain this approach because the initial estimation is competitive.

IV. RESULTS

A. QUANTITATIVE ANALYSIS USING SIMULATED DATA

We test the estimators on the evaluation dataset (see Section III-D) in regions detected with the algorithm described in Section III-E. The ground truth is calculated the same way as in Section III-F. The histograms in Fig. 13 show the distribution of FOIs to actual STDs for the two noise models. Considerably, both distributions are very similar, and most FOIs have an STD less than 2×10^{-4}.

The boxplots in Fig. 14 show the STD estimation errors of the different approaches. The entire box of most estimators is negative, indicating their tendency to underestimate the noise. Additionally, notably, most estimators rarely show any upward outliers. However, the *Pyatykh* and *Smith* approaches have a symmetric distribution of errors around zero.

In terms of the interquartile range (IQR) and the centralized 99%-quantile range ($C_{0.99}R$), the best approaches are *Chen*, *ZoranWeiss*, *Liu*, and *Smith*. Overall, *Chen* achieves the best results; only *Smith* outperforms it on the extended noise model concerning the $C_{0.99}R$.

Similarly, these four estimators perform best concerning the RMSE. Here, the good result of *Smith* derives from its

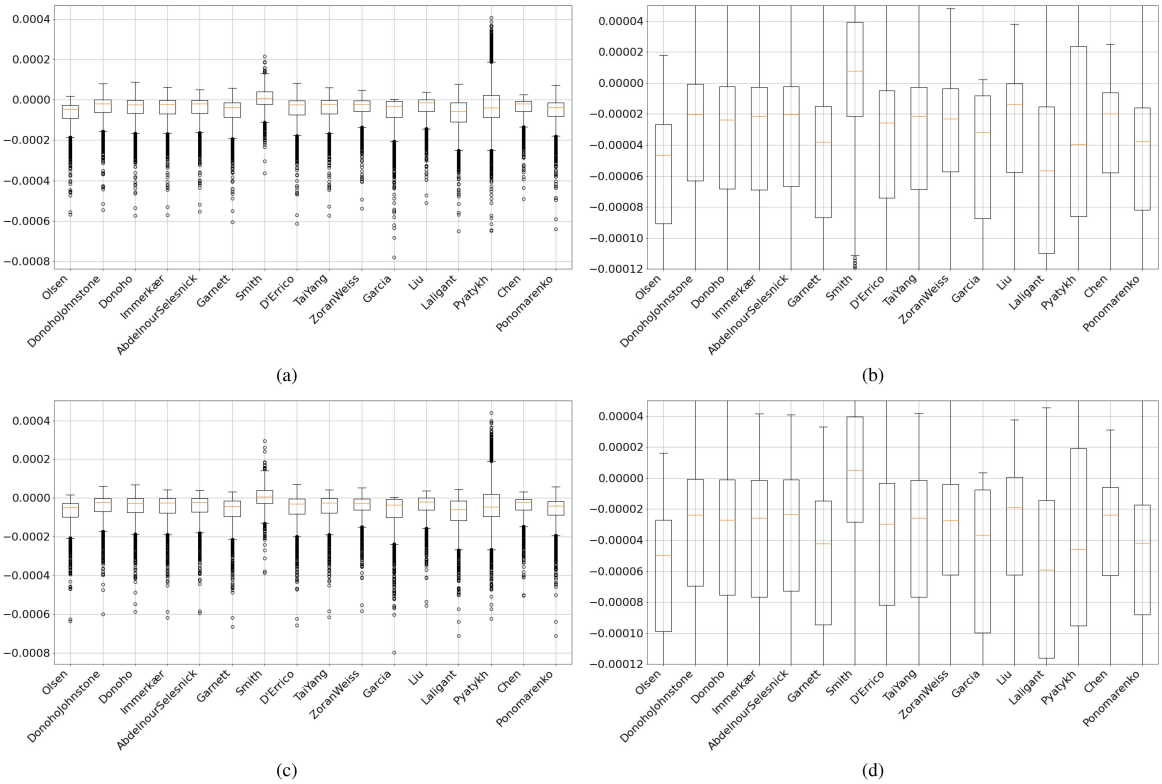

FIGURE 14. **Boxplots of the errors on the evaluation dataset. Each box contains the central 50% of the data, bounded by the upper and lower quartiles. Its length corresponds to the IQR, indicating the dispersion of the data. Furthermore, the red line in the box denotes the median. The whiskers represent the values outside the box, with lengths limited to 1.5 times the IQR. All other values are treated as outliers and marked as dots. (a) Standard noise model. (b) Standard noise model clipped to the box. (c) Extended noise model. (d) Extended noise model clipped to the box.**

mean close to zero and not from a good dispersion. Additionally, Tables 6 and 7 in Appendix C show the values for the quartiles, the associated IQR, the centralized 99%-quantile ($CQ_{0.99}$) interval, the $C_{0.99}R$, and the RMSE.

The scatter plots for the standard noise model in Fig. 15[10] show the estimated and actual STD per FOI for the *Smith*, *Chen*, *Liu*, and *ZoranWeiss* estimators. The *Chen* estimator has the lowest dispersion in compliance with the IQR and $C_{0.99}R$ results. The underestimation of the noise is systematic and, therefore, can be approximately corrected with a compensation term. The *Smith* estimator already uses such a correction term. Additionally, we include investigations on the performance of the estimators on pure AWGN and possible reasons for the underestimation behavior in Appendices A and B.

B. QUALITATIVE EVALUATION: DETECTION OF QUALIFIED REGIONS IN MEASURED DATA

Due to missing ground truth, a quantitative analysis of the estimation errors in the measured data is inapplicable. However, we can evaluate the impact of the estimators on the detection of qualified regions which comprise FOIs satisfying the MSG criterion from (1).

Therefore, we first determine FOIs using the algorithm described in Section III-E. Then, for each FOI, we calculate the local MSG using an estimator to determine the STD of the local noise. Then, we determine the local gradient via a fitted version of the signal as in Section III-A. Finally, we check whether the absolute value of the local gradient consistently exceeds the MSG. If valid, we accept the FOI as a qualified region.

We perform the qualified region detection with the *Chen* (with and without underestimation compensation) and *Pyatykh* estimator to examine their scatter and underestimation influence. Whereas the *Chen* approach shows the lowest dispersion but an underestimation tendency, the *Pyatykh* estimator features the highest dispersion.

The results (see Fig. 16) show that the flanks shift from row to row, forming diagonal wavefronts across several rows. Notably, rejected regions (red) are present where these wavefronts fade out because lower gradients no longer satisfy the MSG criterion. The above behavior is presumably less regular for an estimator with broader dispersion than with smaller dispersion.

Accordingly, the *Chen* estimator produces results without a random acceptance or rejection of FOIs [see Fig.

[10]The plots of the other estimators as well as plots for the extended noise model are included in Figs. 20 and 21 in Appendix C.

IEEE Transactions on Quantum Engineering

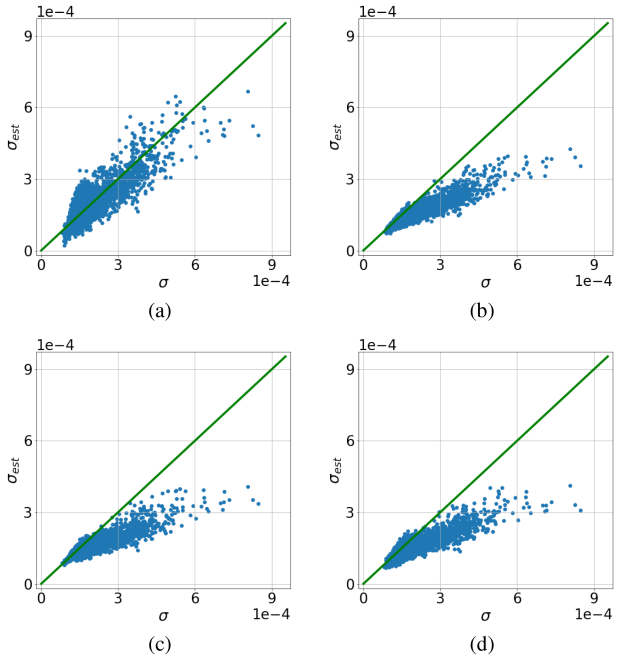

FIGURE 15. Scatter plot (standard noise model) of the actual versus estimated STDs for the estimators of (a) *Smith*, (b) *Chen*, (c) *Liu*, and (d) *ZoranWeiss*. The green line in the figures references a perfect estimate. Each point in the scatter plot represents estimation for one FOI. As expected, the estimates of the *Smith* estimator scatter more evenly, whereas the other estimators tend to underestimate the noise. However, the *Smith* method scatters more strongly than the other estimators.

16(a)]. Moreover, the detection with the *Pyatykh* estimator [see Fig. 16(b)] shows rejections in strong and acceptance in low wavefront areas due to its higher scattering. A reduced signal-to-noise ratio due to the dominant constant noise floor intensifies this behavior in low wavefront areas. To assess the influence of the underestimation, we correct the *Chen* estimator by an approximated compensation derived from the regression line in the examinations on simulated data [see Fig. 16(d)]. Again, the results [see Fig. 16(c)] show no random behavior; only one might observe a negligible amount in the weak parts of the wavefronts.

V. CONCLUSION

This article presents an approach to the noise-sensitive automated tuning of sensor dots in gate-defined semiconductor quantum dots. First, we defined an MSG criterion that requires a local noise estimate to identify qualified regions in sensor dot scans. Subsequently, our evaluation methodology for the estimators comprises a noise analysis, a noise model, the generation of simulated datasets for quantitative analysis, and an optimization of the estimator parameters. Then, the analysis based on the simulated data reveals the quantitative quality characteristics of the estimators and their tendency to underestimate. Finally, on measured data, we showed that a low estimation dispersion is of higher

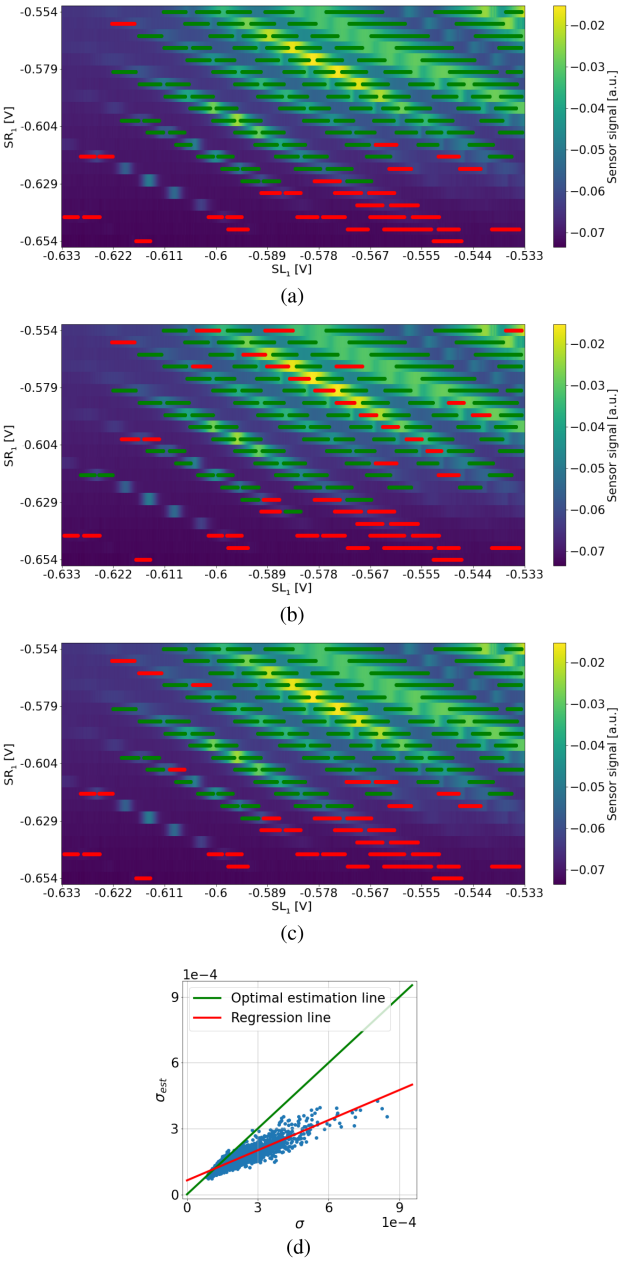

FIGURE 16. Results of the investigation regarding the sensitivity of the quality of results to broader dispersion of the estimation. (a) *Chen* approach, (b) *Pyatykh* approach, and (c) *Chen* approach with approximated compensation. Qualified regions are marked green, and rejected regions are marked red. (d) Regression line in *Chen*'s scatter plot from Fig. 15(b).

relevance for the region identification than the amount of underestimation.

Therefore, when approximately compensating for the underestimation, we propose to use the estimator of Chen et al. [47], as it performs best in terms of dispersion. Additionally, it only needs an average runtime of 0.5 ms[11] per estimated

[11] Using an Intel Xeon E5-2630 v2 - 2.6 GHz.

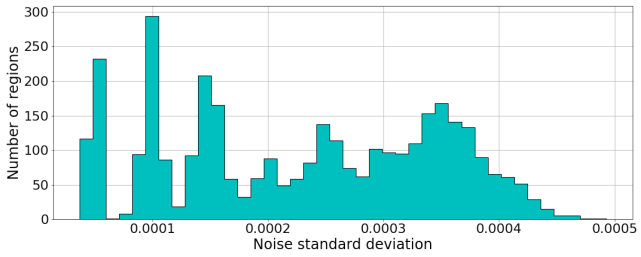

FIGURE 17. Histogram of the distribution of the actual STDs in the FOI found on the evaluation dataset with pure AWGN.

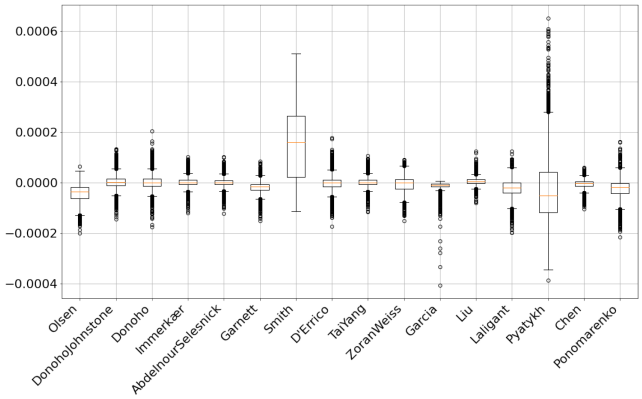

FIGURE 18. Boxplot of errors on the evaluation dataset with pure AWGN.

region and thus is not expected to be a limiting factor in an automated tuning process.

Future research in the automation of the sensor dot tuning needs to address several aspects on basis of the results presented here. Dependent on the different application scenarios such as tuning or readout, a flank selector has to optimize the balance between the flanks' width and steepness. Furthermore, the selector needs to map flanks to wavefronts, identify wavefront irregularities, and evaluate the neighborhood to select the most stable operation area. Additionally, an automated updating of the senor dot to compensate its drifts can significantly improve the quality of the readout data and, thus, ease the automation of subsequent tuning steps. Eventually, all these steps have to tradeoff between complexity, flexibility, and robustness to enable a hardware implementation that will be necessary for a fully functional quantum computer.

VI. DATA AVAILABILITY

The measured sensor dot data that support the findings of this study are available from Jülich DATA with the identifier https://doi.org/10.26165/JUELICH-DATA/QIIBZV. All other data are available from the authors upon reasonable request.

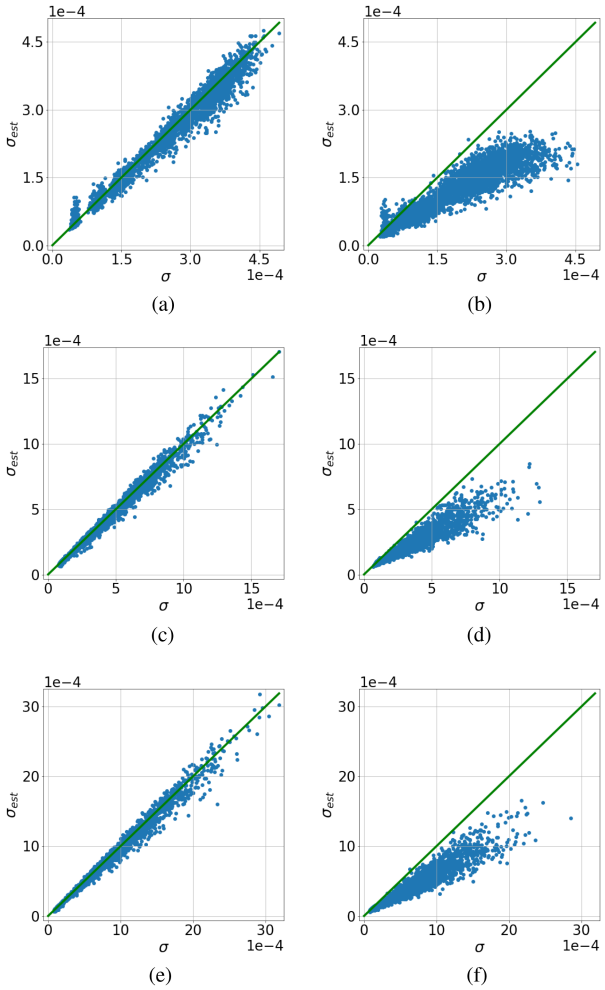

FIGURE 19. Scatter plots of the actual versus the estimated STDs for different noise models. The underestimation does not depend on the regional dependence of the noise but rather on the presence of pink noise. (a) White $\sigma_{\mathbf{const}} = [0.5, 4] \times 10^{-4}$. (b) Pink $\sigma_{\mathbf{const}} = [0.5, 4] \times 10^{-4}$. (c) White $\sigma_{\mathbf{const}} = 10^{-4}$; White $\sigma_{\mathbf{grad}} = 3$. (d) White $\sigma_{\mathbf{const}} = 10^{-4}$; Pink $\sigma_{\mathbf{grad}} = 3$. (e) White $\sigma_{\mathbf{const}} = 10^{-4}$; White $\sigma_{\mathbf{grad}} = 6$. (f) White $\sigma_{\mathbf{const}} = 10^{-4}$; Pink $\sigma_{\mathbf{grad}} = 6$.

APPENDIX A
BEHAVIOR OF ESTIMATORS WITH PURE AWGN

In addition to the tests with the developed noise model, we briefly evaluate the behavior of the estimators with pure AWGN to examine the influence of the type of noise on the estimation quality. Therefore, we add simulated noise with eight different STDs from the interval $[0.5, 4] \times 10^{-5}$ to the smoothed data. Fig. 17 shows the actual distribution of STDs in the FOIs, and Fig. 18 shows the boxplot for the errors of the estimates. No systematic under- or overestimation of the noise occurs for most estimators.

In conclusion, a systematic under- or overestimation strongly depends on the existing noise characteristics. Therefore, this must be considered when developing a compensation strategy to improve the estimation.

IEEE Transactions on Quantum Engineering

TABLE 6. Quartiles, IQR, $CQ_{0.99}$, $C_{0.99}R$, and RMSE for the Error of the Estimates on the Evaluation Dataset With the Standard Noise Model, Sorted Ascending by IQR

Estimator	1st Quartile $[10^{-5}]$	3rd Quartile $[10^{-5}]$	IQR $[10^{-5}]$	$Q_{0.005}$ $[10^{-4}]$	$Q_{0.995}$ $[10^{-5}]$	$C_{0.99}R$ $[10^{-4}]$	RMSE $[10^{-4}]$
Chen	-5.79	-0.63	5.16	-2.60	1.39	2.73	0.65
ZoranWeiss	-5.72	-0.38	5.34	-2.63	3.03	2.93	0.67
Liu	-5.76	-0.04	5.72	-2.70	2.01	2.90	0.66
Smith	-2.14	3.93	6.07	-1.65	12.11	2.87	0.50
DonohoJohnstone	-6.31	-0.06	6.25	-2.86	4.23	3.29	0.73
Olsen	-9.07	-2.68	6.39	-3.26	0.18	3.28	0.93
AbdelnourSelesnick	-6.66	-0.24	6.42	-2.93	2.73	3.20	0.75
Donoho	-6.81	-0.22	6.59	-3.00	4.35	3.43	0.78
Ponomarenko	-8.17	-1.58	6.59	-3.29	3.13	3.61	0.89
Immerkær	-6.88	-0.28	6.61	-2.96	2.74	3.23	0.77
TaiYang	-6.87	-0.26	6.61	-2.95	2.82	3.24	0.77
D'Errico	-7.40	-0.49	6.91	-3.04	4.47	3.49	0.82
Garnett	-8.66	-1.51	7.15	-3.28	2.00	3.48	0.90
Garcia	-8.76	-0.82	7.93	-4.09	0.10	4.10	1.01
Laligant	-10.97	-1.52	9.45	-3.57	3.23	3.89	1.06
Pyatykh	-8.62	2.36	10.98	-3.81	31.62	6.97	1.24

TABLE 7. Quartiles, IQR, $CQ_{0.99}$, $C_{0.99}R$, and RMSE for the Error of the Estimates on the Evaluation Dataset With the Extended Noise Model, Sorted Ascending by IQR

Estimator	1st Quartile $[10^{-5}]$	3rd Quartile $[10^{-5}]$	IQR $[10^{-5}]$	$Q_{0.005}$ $[10^{-4}]$	$Q_{0.995}$ $[10^{-5}]$	$C_{0.99}R$ $[10^{-4}]$	RMSE $[10^{-4}]$
Chen	-6.28	-0.58	5.70	-2.91	1.75	3.08	0.69
ZoranWeiss	-6.26	-0.40	5.85	-3.05	3.52	3.40	0.72
Liu	-6.25	0.06	6.31	-2.96	2.47	3.20	0.70
Smith	-2.84	3.95	6.80	-1.55	13.14	2.86	0.53
DonohoJohnstone	-6.95	-0.08	6.87	-3.19	4.20	3.61	0.77
Ponomarenko	-8.80	-1.72	7.08	-3.65	3.63	4.02	0.94
AbdelnourSelesnick	-7.26	-0.11	7.15	-3.20	2.72	3.47	0.79
Olsen	-9.88	-2.69	7.19	-3.64	0.63	3.70	0.98
Donoho	-7.54	-0.10	7.44	-3.34	4.37	3.77	0.82
Immerkær	-7.66	-0.14	7.52	-3.34	2.92	3.63	0.82
TaiYang	-7.67	-0.13	7.53	-3.33	3.05	3.64	0.82
D'Errico	-8.19	-0.34	7.85	-3.60	3.87	3.99	0.88
Garnett	-9.45	-1.46	7.98	-3.71	1.89	3.89	0.95
Garcia	-9.97	-0.74	9.22	-4.58	0.12	4.59	1.08
Laligant	-11.58	-1.43	10.16	-4.10	3.06	4.40	1.11
Pyatykh	-9.51	1.89	11.41	-4.13	31.23	7.25	1.24

APPENDIX B
SOURCES FOR UNDERESTIMATION

Appendix A shows that underestimation does not occur with pure AWGN. Hence, the noise color and the regional dependence might cause the underestimation. Therefore, we apply different noise models to the evaluation dataset and exemplarily estimate the noise using the *Chen* estimator. Fig. 19 shows the results of the investigation.

Fig. 19(a) and (b) compares the results for independent AWGN and pink n_{const}. The following two figures show the

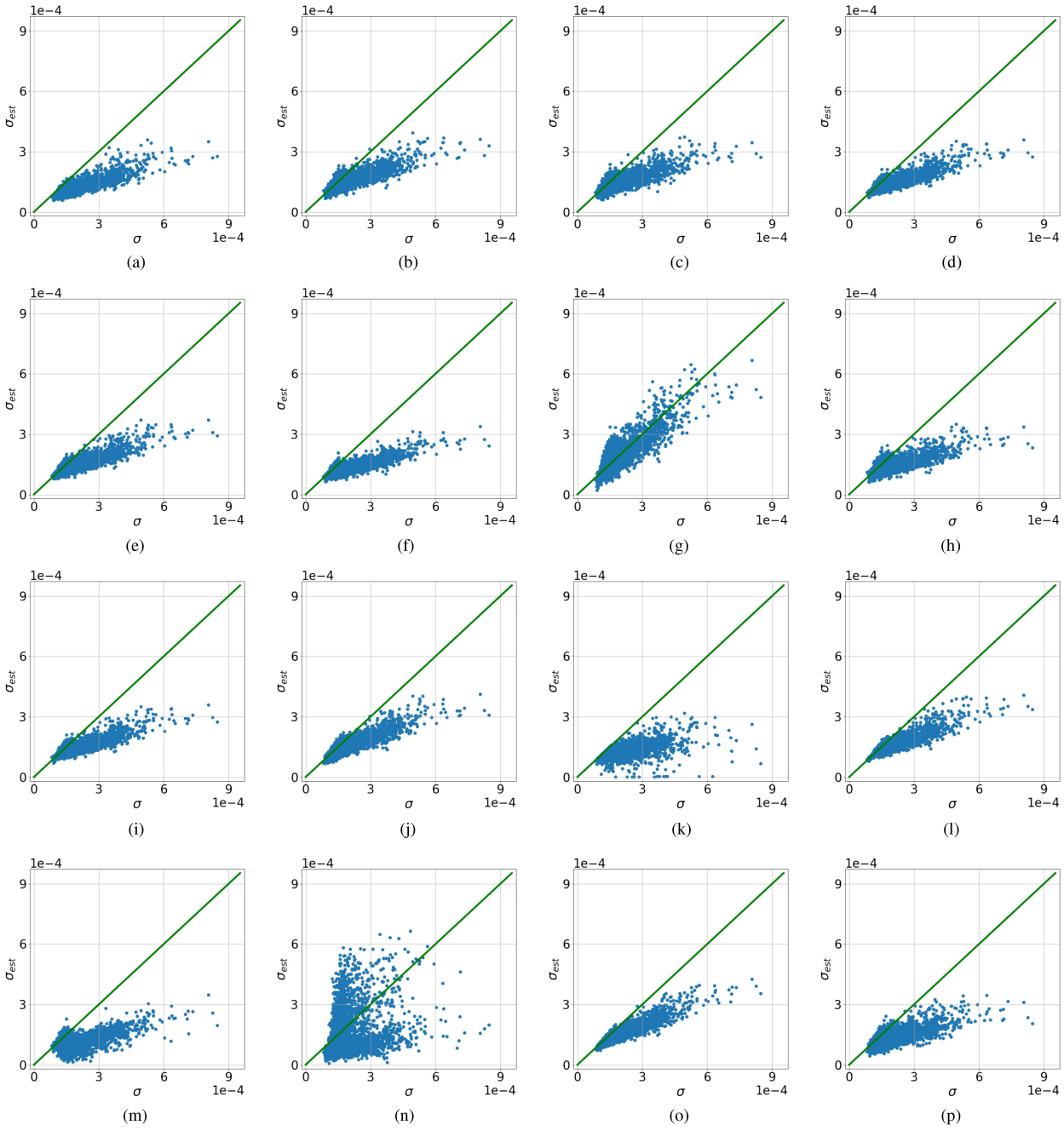

FIGURE 20. Scatter plots of the actual versus the estimated STDs for the evaluation dataset with the standard noise model, sorted in the same order as in Table 4. The green line in the figures indicates where the correct estimate should lie. Each point in the scatter plot represents an FOI. (a) *Olsen*. (b) *DonohoJohnstone*. (c) *Donoho*. (d) *Immerkær*. (e) *AbdelnourSelesnick*. (f) *Garnett*. (g) *Smith*. (h) *D'Errico*. (i) *TaiYang*. (j) *ZoranWeiss*. (k) *Garcia*. (l) *Liu*. (m) *Laligant*. (n) *Pyatykh*. (o) *Chen*. (p) *Ponomarenko*.

results for a noise model consisting of white n_{const} and white n_{grad} [see Fig. 19(c)] and white n_{const} and pink n_{grad} [see Fig. 19(d)], respectively. Finally, Fig. 19(e) and (f) shows results with a more intense gradient component. In all three cases, underestimation only occurs when pink noise is present. In conclusion, the underestimation is not dependent on the regional dependence of the noise but only on the noise color. Accordingly, underestimation compensation presumably requires knowledge of the predominant noise color.

APPENDIX C
SUPPLEMENTARY FIGURES AND TABLES

Tables 6 and 7 show the values for the quartiles, the associated IQR, the $\text{CQ}_{0.99}$ interval, the $C_{0.99}R$, and the RMSE for the error of the estimates on the evaluation dataset. For all tested estimators, Figs. 20 and 21 show the scatter plots of the actual versus the estimated STDs for the evaluation dataset.

IEEE Transactions on Quantum Engineering

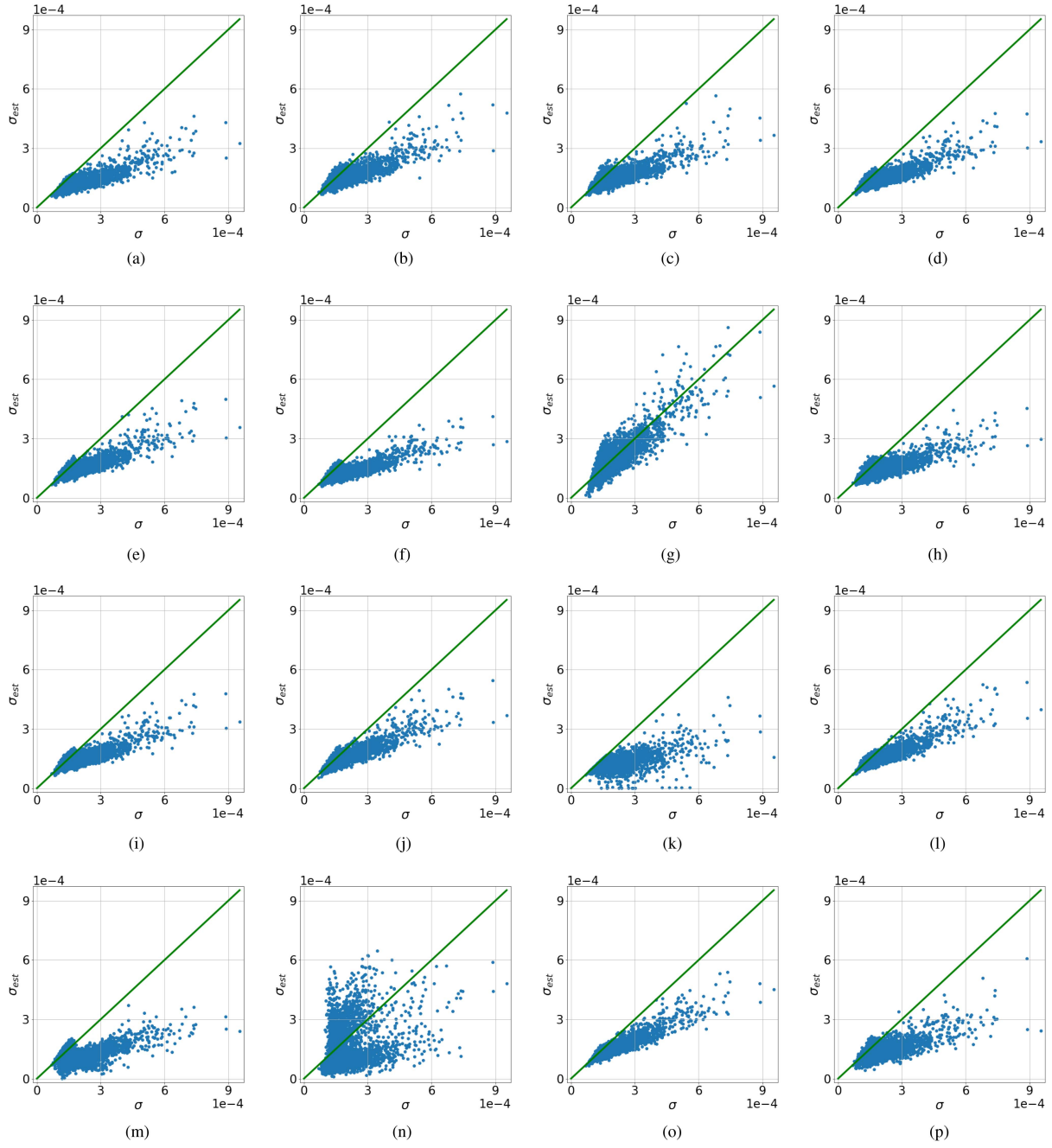

FIGURE 21. **Scatter plots of the actual versus the estimated STDs for the evaluation dataset with the extended noise model, sorted in the same order as in Table 4. The green line in the figures indicates where the correct estimate should lie. Each point in the scatter plot represents an FOI. (a) *Olsen*. (b) *DonohoJohnstone*. (c) *Donoho*. (d) *Immerkær*. (e) *AbdelnourSelesnick*. (f) *Garnett*. (g) *Smith*. (h) *D'Errico*. (i) *TaiYang*. (j) *ZoranWeiss*. (k) *Garcia*. (l) *Liu*. (m) *Laligant*. (n) *Pyatykh*. (o) *Chen*. (p) *Ponomarenko*.**

REFERENCES

[1] R. Hanson, L. P. Kouwenhoven, J. R. Petta, S. Tarucha, and L. M. K. Vandersypen, "Spins in few-electron quantum dots," *Rev. Modern Phys.*, vol. 79, no. 4, pp. 1217–1265, Oct. 2007, doi: 10.1103/RevModPhys.79.1217.

[2] R. S. Smith, M. J. Curtis, and W. J. Zeng, "A practical quantum instruction set architecture," Feb. 2017, *arXiv:1608.03355*, doi: 10.48550/arXiv.1608.03355.

[3] W. G. van der Wiel, S. De Franceschi, J. M. Elzerman, T. Fujisawa, S. Tarucha, and L. P. Kouwenhoven, "Electron transport through double quantum dots," *Rev. Modern Phys.*, vol. 75, no. 1, pp. 1–22, Dec. 2002, doi: 10.1103/RevModPhys.75.1.

[4] T. Botzem, "Coherence and high fidelity control of two-electron spin qubits in GaAs quantum dots," Ph.D. dissertation, Dept. Phys., RWTH Aachen, Aachen, Germany, Jan. 2017, doi: 10.18154/RWTH-2017-04410.

[5] P. Cerfontaine, "High-fidelity single- and two-qubit gates for two-electron spin qubits," Ph.D. dissertation, Dept. Phys., RWTH Aachen Univ., Aachen, Germany, Jul. 2019, doi: 10.18154/RWTH-2019-09348.

[6] O. E. Dial, M. D. Shulman, S. P. Harvey, H. Bluhm, V. Umansky, and A. Yacoby, "Charge noise spectroscopy using coherent exchange oscillations in a singlet-triplet qubit," *Phys. Rev. Lett.*, vol. 110, no. 14, Apr. 2013, Art. no. 146804, doi: 10.1103/PhysRevLett.110.146804.

[7] E. Paladino, Y. M. Galperin, G. Falci, and B. L. Altshuler, "1/F noise: Implications for solid-state quantum information," *Rev. Modern Phys.*, vol. 86, no. 2, pp. 361–418, Apr. 2014, doi: 10.1103/RevModPhys.86.361.

[8] E. J. Connors, J. Nelson, L. F. Edge, and J. M. Nichol, "Charge-noise spectroscopy of Si/SiGe quantum dots via dynamically-decoupled exchange oscillations," *Nature Commun.*, vol. 13, no. 1, Dec. 2022, Art. no. 940, doi: 10.1038/s41467-022-28519-x.

[9] T. Struck et al., "Low-frequency spin qubit energy splitting noise in highly purified ^{28}Si/SiGe," *npj Quantum Inf.*, vol. 6, no. 1, Dec. 2020, Art. no. 40, doi: 10.1038/s41534-020-0276-2.

[10] J. R. Barry, E. A. Lee, and D. G. Messerschmitt, *Digital Communication*, 3rd ed. Boston, MA, USA: Springer, 2004, doi: 10.1007/978-1-4615-0227-2.

[11] T. A. Baart, L. M. K. Vandersypen, P. T. Eendebak, C. Reichl, and W. Wegscheider, "Computer-automated tuning of semiconductor double quantum dots into the single-electron regime," *Appl. Phys. Lett.*, vol. 108, no. 21, May 2016, Art. no. 213104, doi: 10.1063/1.4952624.

[12] S. N. R. Uppuluru, "Automated coarse tuning of quantum sensor dots," Master's thesis, Inst. Comput. Sci., Georg-August-Universität, Göttingen, Germany, Oct. 2021.

[13] D. T. Lennon et al., "Efficiently measuring a quantum device using machine learning," *npj Quantum Inf.*, vol. 5, no. 1, Dec. 2019, Art. no. 79, doi: 10.1038/s41534-019-0193-4.

[14] V. Nguyen et al., "Deep reinforcement learning for efficient measurement of quantum devices," *npj Quantum Inf.*, vol. 7, no. 1, pp. 1–9, Jun. 2021, doi: 10.1038/s41534-021-00434-x.

[15] J. P. Zwolak and J. M. Taylor, "Colloquium: Advances in automation of quantum dot devices control," *Rev. Modern Phys.*, vol. 95, 2023, Art. no. 011006, doi: 10.1103/RevModPhys.95.011006.

[16] V. P. Tuzlukov, *Signal Processing Noise* , 1st ed. ser. The Electrical Engineering and Applied Signal Processing Series. Boca Raton, FL, USA: CRC, 2002, doi: 10.1201/9781315220147.

[17] S. M. Kay, *Fundamentals of Statistical Signal Processing*. ser. Prentice Hall Signal Processing Series. Englewood Cliffs, NJ, USA: Prentice-Hall, 1993.

[18] C.-Y. Chi, C.-C. Feng, C.-H. Chen, and C.-Y. Chen, "Fundamentals of statistical signal processing," in *Blind Equalization and System Identification: Batch Processing Algorithms, Performance and Applications*, C.-Y. Chi, Ed., London, U.K.:Springer, 2006, pp. 83–180, doi: 10.1007/1-84628-218-7_3.

[19] G. Luo and D. Zhang, "Wavelet denoising," in *Advances in Wavelet Theory and Their Applications in Engineering, Physics and Technology*, D. Baleanu, Ed. London, U.K.: InTech, 2012, pp. 59–80, doi: 10.5772/37424.

[20] R. Pandya and K. Pathak, "Survey on noise estimation and removal methods through SVM," *Int. J. Comput. Appl.*, vol. 86, no. 9, pp. 25–32, Jan. 2014, doi: 10.5120/15014-3297.

[21] W. Liu and W. Lin, "Additive white Gaussian noise level estimation in SVD domain for images," *IEEE Trans. Image Process.*, vol. 22, no. 3, pp. 872–883, Mar. 2013, doi: 10.1109/TIP.2012.2219544.

[22] W. Liu, "Additive white Gaussian noise level estimation based on block SVD," in *Proc. IEEE Workshop Electron., Comput., Appl.*, 2014, pp. 960–963, doi: 10.1109/IWECA.2014.6845781.

[23] A. Khmag, A. R. Ramli, S. A. R. Al-haddad, and N. Kamarudin, "Natural image noise level estimation based on local statistics for blind noise reduction," *Vis. Comput.*, vol. 34, no. 4, pp. 575–587, Apr. 2018, doi: 10.1007/s00371-017-1362-0.

[24] S. I. Olsen, "Estimation of noise in images: An evaluation," *CVGIP: Graphical Models Image Process.*, vol. 55, no. 4, pp. 319–323, 1993, doi: 10.1006/cgip.1993.1022.

[25] J. Immerkær, "Fast noise variance estimation," *Comput. Vis. Image Understanding*, vol. 64, no. 2, pp. 300–302, Sep. 1996, doi: 10.1006/cviu.1996.0060.

[26] B. R. Corner, R. M. Narayanan, and S. E. Reichenbach, "Noise estimation in remote sensing imagery using data masking," *Int. J. Remote Sens.*, vol. 24, no. 4, pp. 689–702, Jan. 2003, doi: 10.1080/01431160210164271.

[27] T.-A. Nguyen and M.-C. Hong, "Filtering-based noise estimation for denoising the image degraded by Gaussian noise," in *Advances in Image and Video Technology*, Y.-S. Ho, Ed., Berlin, Germany: Springer, 2011, vol. 7088, pp. 157–167, doi: 10.1007/978-3-642-25346-1_15.

[28] R. Garnett, T. Huegerich, C. Chui, and W. He, "A universal noise removal algorithm with an impulse detector," *IEEE Trans. Image Process.*, vol. 14, no. 11, pp. 1747–1754, Nov. 2005, doi: 10.1109/TIP.2005.857261.

[29] J. D'Errico, "Estimatenoise," 2007. [Online]. Available: https://www.mathworks.com/matlabcentral/fileexchange/16683-estimatenoise

[30] O. Laligant, F. Truchetet, and E. Fauvet, "Noise estimation from digital step-model signal," *IEEE Trans. Image Process.*, vol. 22, no. 12, pp. 5158–5167, Dec. 2013, doi: 10.1109/TIP.2013.2282123.

[31] S. M. Mousavi and C. A. Langston, "Adaptive noise estimation and suppression for improving microseismic event detection," *J. Appl. Geophys.*, vol. 132, pp. 116–124, Sep. 2016, doi: 10.1016/j.jappgeo.2016.06.008.

[32] N. u Rehman, B. Khan, and K. Naveed, "Data-driven multivariate signal denoising using Mahalanobis distance," *IEEE Signal Process. Lett.*, vol. 26, no. 9, pp. 1408–1412, Sep. 2019, doi: 10.1109/LSP.2019.2932715.

[33] K. Rank, M. Lendl, and R. Unbehauen, "Estimation of image noise variance," *Proc. Inst. Elect. Eng.—Vis., Image Signal, Process.*, vol. 146, no. 2, pp. 80–84, Apr. 1999, doi: 10.1049/ip-vis:19990238.

[34] A. Bosco, A. Bruna, G. Messina, and G. Spampinato, "Fast method for noise level estimation and integrated noise reduction," *IEEE Trans. Consum. Electron.*, vol. 51, no. 3, pp. 1028–1033, Aug. 2005, doi: 10.1109/TCE.2005.1510518.

[35] S.-C. Tai and S.-M. Yang, "A fast method for image noise estimation using Laplacian operator and adaptive edge detection," in *Proc. 3rd Int. Symp. Commun., Control, Signal Process.*, 2008, pp. 1077–1081, doi: 10.1109/ISCCSP.2008.4537384.

[36] S.-M. Yang, "Fast and reliable image-noise estimation using a hybrid approach," *J. Electron. Imag.*, vol. 19, no. 3, Art. no. 033007, Jul. 2010, doi: 10.1117/1.3476329.

[37] U. Schmidt, K. Schelten, and S. Roth, "Bayesian deblurring with integrated noise estimation," in *Proc. IEEE/CVF Conf. Comput. Vis. Pattern Recognit.*, Jun. 2011, pp. 2625–2632, doi: 10.1109/CVPR.2011.5995653.

[38] C. Sutour, C.-A. Deledalle, and J.-F. Aujol, "Estimation of the noise level function based on a nonparametric detection of homogeneous image regions," *SIAM J. Imag. Sci.*, vol. 8, no. 4, pp. 2622–2661, Jan. 2015, doi: 10.1137/15M1012682.

[39] S. Pyatykh and J. Hesser, "Image sensor noise parameter estimation by variance stabilization and normality assessment," *IEEE Trans. Image Process.*, vol. 23, no. 9, pp. 3990–3998, Sep. 2014, doi: 10.1109/TIP.2014.2339194.

[40] J. Lee and K. Hoppel, "Noise modeling and estimation of remotely-sensed images," in *Proc. 12th Can. Symp. Remote Sens. Geosci. Remote Sens. Symp.*, 1989, pp. 1005–1008, doi: 10.1109/IGARSS.1989.579061.

[41] S. Pyatykh, J. Hesser, and L. Zheng, "Image noise level estimation by principal component analysis," *IEEE Trans. Image Process.*, vol. 22, no. 2, pp. 687–699, Feb. 2013, doi: 10.1109/TIP.2012.2221728.

[42] D.-H. Shin, R.-H. Park, S. Yang, and J.-H. Jung, "Block-based noise estimation using adaptive Gaussian filtering," *IEEE Trans. Consum. Electron.*, vol. 51, no. 1, pp. 218–226, Feb. 2005, doi: 10.1109/TCE.2005.1405723.

[43] M. Rakhshanfar and M. A. Amer, "Estimation of Gaussian, Poissonian-Gaussian, and processed visual noise and its level function," *IEEE Trans. Image Process.*, vol. 25, no. 9, pp. 4172–4185, Sep. 2016, doi: 10.1109/TIP.2016.2588320.

[44] A. Amer and E. Dubois, "Fast and reliable structure-oriented video noise estimation," *IEEE Trans. Circuits Syst. Video Technol.*, vol. 15, no. 1, pp. 113–118, Jan. 2005, doi: 10.1109/TCSVT.2004.837017.

[45] X. Liu, M. Tanaka, and M. Okutomi, "Noise level estimation using weak textured patches of a single noisy image," in *Proc. IEEE 19th Int. Conf. Image Process.*, 2012, pp. 665–668, doi: 10.1109/ICIP.2012.6466947.

[46] X. Liu, M. Tanaka, and M. Okutomi, "Single-image noise level estimation for blind denoising," *IEEE Trans. Image Process.*, vol. 22, no. 12, pp. 5226–5237, Dec. 2013, doi: 10.1109/TIP.2013.2283400.

[47] G. Chen, F. Zhu, and P. A. Heng, "An efficient statistical method for image noise level estimation," in *Proc. IEEE Int. Conf. Comput. Vis.*, 2015, pp. 477–485, doi: 10.1109/ICCV.2015.62.

[48] M. Colom and A. Buades, "Analysis and extension of the PCA method, estimating a noise curve from a single image," *Image Process. On Line*, vol. 5, pp. 365–390, Dec. 2016, doi: 10.5201/ipol.2016.124.

[49] P. Jiang and J.-z. Zhang, "Fast and reliable noise level estimation based on local statistic," *Pattern Recognit. Lett.*, vol. 78, pp. 8–13, Jul. 2016, doi: 10.1016/j.patrec.2016.03.026.

[50] Z. Fang and X. Yi, "A novel natural image noise level estimation based on flat patches and local statistics," *Multimedia Tools Appl.*, vol. 78, no. 13, pp. 17337–17358, Jul. 2019, doi: 10.1007/s11042-018-7137-4.

[51] D. L. Donoho and I. M. Johnstone, "Ideal spatial adaptation by wavelet shrinkage," *Biometrika*, vol. 81, no. 3, pp. 425–455, Sep. 1994, doi: 10.1093/biomet/81.3.425.

[52] D. L. Donoho, "De-noising by soft-thresholding," *IEEE Trans. Inf. Theory*, vol. 41, no. 3, pp. 613–627, May 1995, doi: 10.1109/18.382009.

[53] A. Abdelnour and I. Selesnick, "Design of 2-band orthogonal near-symmetric CQF," in *Proc. IEEE Int. Conf. Acoust., Speech, Signal Process.*, 2001, vol. 6, pp. 3693–3696, doi: 10.1109/ICASSP.2001.940644.

[54] A. De Stefano, P. White, and W. Collis, "Training methods for image noise level estimation on wavelet components," *EURASIP J. Adv. Signal Process.*, vol. 2004, no. 16, Dec. 2004, Art. no. 405209, doi: 10.1155/S1110865704401218.

[55] K. Naveed, B. Shaukat, and N. ur Rehman, "Signal denoising based on dual tree complex wavelet transform and goodness of fit test," in *Proc. 22nd Int. Conf. Digit. Signal Process.*, 2017, pp. 1–5, doi: 10.1109/ICDSP.2017.8096067.

[56] E. F. Smith, "Development of an image noise estimation method and a sub-imaging based wiener method," Ph.D. dissertation, Dept. Phys., Univ. New Orleans, Theses Dissertations, New Orleans, LA, USA, Dec. 2006. [Online]. Available: https://scholarworks.uno.edu/td/1052

[57] N. N. Ponomarenko, V. V. Lukin, S. K. Abramov, K. O. Egiazarian, and J. T. Astola, "Blind evaluation of additive noise variance in textured images by nonlinear processing of block DCT coefficients," *Proc. SPIE*, vol. 5014, pp. 178–189, May 2003, doi: 10.1117/12.477717.

[58] M. Lebrun, M. Colom, and J.-M. Morel, "The noise clinic: A blind image denoising algorithm," *Image Process. Online*, vol. 5, pp. 1–54, Jan. 2015, doi: 10.5201/ipol.2015.125.

[59] N. N. Ponomarenko, N. Gapon, V. Voronin, and K. Egiazarian, "Blind estimation of white Gaussian noise variance in highly textured images," 2017, *arXiv: 1711.10792*, doi: 10.48550/arxiv.1711.10792.

[60] M. Colom and A. Buades, "Analysis and extension of the Ponomarenko et al. method, estimating a noise curve from a single image," *Image Process. Online*, vol. 3, pp. 173–197, Jul. 2013, doi: 10.5201/ipol.2013.45.

[61] D. Zoran and Y. Weiss, "Scale invariance and noise in natural images," in *Proc. IEEE 12th Int. Conf. Comput. Vis.*, 2009, pp. 2209–2216, doi: 10.1109/ICCV.2009.5459476.

[62] D. Garcia, "Robust smoothing of gridded data in one and higher dimensions with missing values," *Comput. Statist. Data Anal.*, vol. 54, no. 4, pp. 1167–1178, Apr. 2010, doi: 10.1016/j.csda.2009.09.020.

[63] S. Kafanov, H. Brenning, T. Duty, and P. Delsing, "Charge noise in single-electron transistors and charge qubits may be caused by metallic grains," *Phys. Rev. B*, vol. 78, no. 12, Sep. 2008, Art. no. 125411, doi: 10.1103/PhysRevB.78.125411.

[64] G. Breit and E. Wigner, "Capture of slow neutrons," *Phys. Rev.*, vol. 49, no. 7, pp. 519–531, Apr. 1936, doi: 10.1103/PhysRev.49.519.

[65] L. P. Kouwenhoven, C. M. Marcus, P. L. McEuen, S. Tarucha, R. M. Westervelt, and N. S. Wingreen, "Electron transport in quantum dots," in *Mesoscopic Electron Transport*, L. L. Sohn, L. P. Kouwenhoven, and G. Schön, Eds. Dordrecht, The Netherlands:Springer, 1997, pp. 105–214, doi: 10.1007/978-94-015-8839-3_4.

[66] M. E. O'Neill, "PCG: A family of simple fast space-efficient statistically good algorithms for random number generation," Harvey Mudd College, Claremont, CA, Tech. Rep. HMC-CS-2014-0905, Sep. 2014. [Online]. Available: https://www.cs.hmc.edu/tr/hmc-cs-2014-0905.pdf

[67] J. Timmer and M. König, "On generating power law noise," *Astron. Astrophys.*, vol. 300, pp. 707–710, Aug. 1995. [Online]. Available: https://adsabs.harvard.edu/full/1995A%26A...300..707

[68] O. Laligant, "Noise estimator / estimation for various types of noise," Apr. 2020. Accessed: Jun. 2, 2021. [Online]. Available: https://de.mathworks.com/matlabcentral/fileexchange/63172-noise-estimator-estimation-for-various-types-of-noise

[69] A. Foi, "function_stdEst," Dept. Signal Process., Tampere Univ. Technol., 2011. Accessed: Jun. 30, 2021. [Online]. Available: https://webpages.tuni.fi/lasip/2D/LASIP_Image_Restoration_DemoBox_v120.zip

[70] S. Fleitmann, "estimate_noise_std," Central Inst. Eng., Electron., Analytics - Electron. Syst., Forschungszentrum Jülich GmbH, Jülich, Germany, 2020, available on request: s.fleitmann, fz-juelich.de.

[71] D. Zoran and Y. Weiss, "estimateNoiseSDUsingKurts," Hebrew Univ. Jerusalem, Jerusalem, Israel, 2009. Accessed: Jun. 1, 2021. [Online]. Available: https://people.csail.mit.edu/danielzoran/noiseestimation.zip

[72] D. Garcia, "Noise variance estimation," Jun. 2020. Accessed: Jul. 7, 2021. [Online]. Available: https://www.mathworks.com/matlabcentral/fileexchange

[73] C. Schwemmer, "Noiseest_matlab," Friedrich-Alexander-Universität, Pattern Recognition Lab, Erlangen-Nürnberg, Dec. 2019. Accessed: Jun. 15, 2021. [Online]. Available: https://www5.cs.fau.de/fileadmin/Persons/SchwemmerChris/noiseest_matlab.zip

[74] M. Tanaka, "Noise level estimation from a single image," Feb. 2015. Accessed: Jun. 3, 2021. [Online]. Available: https://de.mathworks.com/matlabcentral/fileexchange/36921-noise-level-estimation-from-a-single-image

[75] S. Pyatykh, "PCANoiseLevelEstimator," Heidelberg University, Medical Faculty Mannheim, Mannheim Institute for Intelligent Systems in Medicine (MIISM), Heidelberg, 2013. Accessed: Jun. 2, 2021. [Online]. Available: http://physics.medma.uni-heidelberg.de/cms/sites/default/files/img/Stanislav/noise_param_estimation/2013_noise_level_estimation.zip

[76] Z. Yue, "Noise_estimation," Apr. 2020. Accessed: Jun. 2, 2021. [Online]. Available: https://github.com/zsyOAOA/noise_est_ICCV2015

[77] C. Sutour, "Noise_estimation," Sep. 2015. [Online]. Available: https://github.com/csutour/RNLF/tree/master/noisetools

[78] N. N. Ponomarenko, "IEDD," Tampere Univ. Technol., Dept. Signal Process., Tampere, Finland, 2017. Accessed: Jun. 31, 2021. [Online]. Available: https://ponomarenko.info/iedd.html

Fabian Hader received the B.Sc. degree in scientific programming and the M.Sc. degree in energy economics and informatics from FH Aachen—University of Applied Sciences, Jülich, Germany, in 2019 and 2021, respectively. He is currently working toward the Ph.D. degree in engineering with the University Duisburg-Essen, Duisburg/Essen, Germany.

From 2019 to 2021, he was a Software Engineer with the Central Institute of Engineering, Electronics, and Analytics - Electronic Systems, Forschungszentrum Jülich GmbH, Jülich. His research interest focuses on the automatic tuning of quantum dots.

Jan Vogelbruch received the Dipl.Ing. and Dr.-Ing. degrees in electrical engineering from RWTH Aachen University, Aachen, Germany, in 1994 and 2003, respectively.

In 1995, he joined Parsytec Computer GmbH, Aachen, as a Technical Project Manager for European cooperations. His focus has been on high-performance computing and image processing solutions, where he has been the Technical Leader for the company's part in several EC-funded projects. Since late 1998, he has been with the Central Institute of Engineering, Electronics, and Analytics - Electronic Systems at Forschungszentrum Jülich GmbH, Jülich, Germany. His research interests include parallel computing, signal and 3-D image processing, fast reconstruction methods for high-resolution computer tomography, and automated defect detection. His current research interest focuses on the automatic tuning of semiconductor quantum dots.

Simon Humpohl received the B.Sc. and M.Sc. degrees in physics in 2014 and 2017, respectively, from RWTH Aachen University, Aachen, Germany, where he is currently working toward the doctoral degree under the supervision of Prof. Hendrik Bluhm at the JARA Institute for Quantum Information.

His research focuses on the tuning and operation of electron spin qubits in semiconductor quantum dots.

Tobias Hangleiter received the B.Sc. and M.Sc. degrees in physics in 2016 and 2019, respectively, from RWTH Aachen University, Aachen, Germany, where he is currently working toward the doctoral degree in quantum technology with 2nd Institute of Physics.

His research interests include the automatic tuning of semiconductor quantum dots, quantum dynamics in the presence of correlated noise, and optical interfaces for semiconductor spin qubits.

Chimezie Eguzo received the M.Sc. degree in microelectronics and wireless systems from Coventry University, Coventry, U.K., in 2014.

In 2019, he joined the Central Institute of Engineering, Electronics and Analytics ZEA-2 Electronic Systems, Forschungszentrum Jülich, Jülich, Germany, where he is currently working on information and embedded systems. His research focuses on automating the build process and configuring the cross-compilation environment for different processing system architectures.

Stefan Heinen received the diploma and doctoral degrees in electrical engineering from the Aachen University of Technology, Aachen, Germany, in 1994 and 2001, respectively.

In 2000, he joined Synopsys, working on the development of digital receiver algorithms for 2.5G, 3G, and GPS. His focus was on the algorithmic exploration and modeling methodology of HW/SW architectures. In 2004, he was a Virtual Prototype Architect with Infineon's mobile phone division, defining the model-driven design flow of Infineon's 3G/3.5G cell phone modem that later became part of the first iPhones. After the merger of Infineon's mobile business with Intel in 2011, he contributed to the definition of channel decoding and receiver algorithms for Intel's 4G and 5G cell phone modems. Since 2020, he has been with Helmholtz Research Center, Jülich, Germany. His research interests include speech and channel coding, error-robust parameter estimation, and digital signal processing algorithms applied to various fields, such as RF-based object localization and quantum computing.

Stefanie Meyer received the B.Sc. degree in scientific programming and the M.Sc. degree in technomathematics from FH Aachen-University of Applied Sciences, Jülich, Germany, in 2011 and 2013, respectively.

In 2008, she joined the Institute of Energy and Climate Research - Fuel Cells, Forschungszentrum Jülich GmbH, Jülich. Her research included developing and parallelizing high-temperature polymer electrolyte fuel cell models for HPC. Since 2014, she has been the head of the software development team with the Central Institute of Engineering, Electronics, and Analytics - Electronic Systems, Forschungszentrum Jülich GmbH. Her research interests have a particular focus on electronic systems for quantum computing.

Stefan van Waasen received the diploma and doctor's degrees in electrical engineering from Gerhard-Mercator University, Duisburg, Germany, in 1994 and 1999, respectively. The topic of his doctoral thesis was optical receivers up to 60 Gb/s based on traveling wave amplifiers.

In 1998, he joined Siemens Semiconductors/Infineon Technologies AG, Düsseldorf, Germany. His responsibility was BiCMOS and CMOS RF system development for highly integrated cordless systems such as DECT and Bluetooth. In 2001, he changed into the IC development of front-end systems for high data rate optical communication systems. From 2004 to 2006, he was with Stockholm Design Center responsible for the short-range analog, mixed-signal, and RF development for SoC CMOS solutions. From 2006 to 2010, he was responsible for the wireless RF system engineering in the area of SoC CMOS products at the headquarters in Munich, Germany, and later in the Design Center Duisburg, Duisburg. Since 2010, he has been the Director of the Central Institute of Engineering, Electronics, and Analytics - Electronic Systems at Forschungszentrum Jülich GmbH, Jülich, Germany. In 2014, he became a Professor for measurement and sensor systems with the Communication Systems Chair, University of Duisburg-Essen. His research interests include complex measurement and detector systems, particularly focusing on electronic systems for quantum computing.